OXFORD

Cerebral Cortex, April 2016;26: 1512–1528

doi: 10.1093/cercor/bhu317
Advance Access Publication Date: 16 January 2015
Original Article

ORIGINAL ARTICLE

Altered Functionality, Morphology, and Vesicular Glutamate Transporter Expression of Cortical Motor Neurons from a Presymptomatic Mouse Model of Amyotrophic Lateral Sclerosis

L. Saba[1,†], M. T. Viscomi[1,†], S. Caioli[1], A. Pignataro[1], E. Bisicchia[1], M. Pieri[2], M. Molinari[1], M. Ammassari-Teule[1,3], and C. Zona[1,2]

[1]I.R.C.C.S. Fondazione S. Lucia, Rome 00143, Italy, [2]Department of Systems Medicine, University of Rome "Tor Vergata," Rome 00133, Italy, and [3]Institute of Cell Biology and Neurobiology, National Research Council, Rome 00143, Italy

Address correspondence to Cristina Zona, Department of Systems Medicine, University of Rome "Tor Vergata," Via Montpellier, 1, Rome 00 133, Italy. Email: zona@uniroma2.it

[†]L.S. and M.T.V. contributed equally to this work.

Abstract

Amyotrophic lateral sclerosis (ALS) is a lethal disorder characterized by the gradual degeneration of motor neurons in the cerebrospinal axis. Whether upper motor neuron hyperexcitability, which is a feature of ALS, provokes dysfunction of glutamate metabolism and degeneration of lower motor neurons via an anterograde process is undetermined. To examine whether early changes in upper motor neuron activity occur in association with glutamatergic alterations, we performed whole-cell patch-clamp recordings to analyze excitatory properties of Layer V cortical motor neurons and excitatory postsynaptic currents (EPSCs) in presymptomatic G93A mice modeling familial ALS (fALS). We found that G93A Layer V pyramidal neurons exhibited altered EPSC frequency and rheobase values indicative of their hyperexcitability status. Biocytin loading of these hyperexcitable neurons revealed an expansion of their basal dendrite arborization. Moreover, we detected increased expression levels of the vesicular glutamate transporter 2 in cortical Layer V of G93A mice. Altogether our data show that functional and structural neuronal alterations associate with abnormal glutamatergic activity in motor cortex of presymptomatic G93A mice. These abnormalities, expected to enhance glutamate release and to favor its accumulation in the motor cortex, provide strong support for the view that upper motor neurons are involved early on in the pathogenesis of ALS.

Key words: excitatory neurotransmission, G93A mice, motor neuron hyperexcitability, neuronal morphology, vesicular glutamate transporter

Introduction

Amyotrophic lateral sclerosis (ALS) is a lethal adult-onset neurological disease characterized by degeneration of the upper and lower motor neurons (Wijesekera and Leigh 2009; Kiernan et al. 2011). The etiology of the disease remains elusive. Most cases of ALS are sporadic (sALS), whereas familial ALS (fALS) constitutes ~5–10% of ALS cases and is usually inherited in an autosomal dominant manner. Mutations in Cu/Zn superoxide dismutase enzyme (SOD1) (Deng et al. 1993; Rosen et al. 1993; Moreira et al. 2013) account for approximately ~30% of fALS. Notably,

the G93A transgenic mouse, which overexpresses the mutated human *sod1* gene in which glycine is substituted by alanine at residue 93, shows clinical signs that closely mimic human ALS and is the most characterized mouse model of ALS (Gurney 1994; Andersen 2006). In particular, G93A mice develop hindlimb tremor and weakness at around 3 months detected by locomotor deficits, progressing to hyper-reflexia, paralysis, and premature death after 4 months (Gurney 1994).

The pathophysiological mechanisms triggering motor neuron vulnerability in ALS arises from a combination of mechanisms, including environmental toxicity (Van Den Bosch et al. 2006; Foran and Trotti 2009), mitochondrial dysfunction (Grosskreutz et al. 2007), oxidative damage (Panov et al. 2011), aberrant protein aggregation (Vance et al. 2009), deregulation of Ca^{2+} homeostasis (Guatteo et al. 2007; Martorana et al. 2012), immune system deficiency and neuroinflammation (Alexianu et al. 2001; Philips and Robberecht 2011), and altered functionality of neuronal ionic channels and excitability (Kuo et al. 2005; Zona et al. 2006; Pieri et al. 2009; Carunchio et al. 2010; Vucic, Ziemann et al. 2013). However, many of these abnormalities have been linked to an excitotoxicity cascade that involves the glutamatergic neurotransmitter system, with the accumulation of glutamate leading to an excessive activation of glutamate receptors at the synaptic cleft (Foran et al. 2011; Spalloni et al. 2011). Indeed, an enhanced glutamate concentration in the cortex could have repercussions on the expression of vesicular glutamate transporters (VGluTs), which regulate the re-uptake of glutamate in their secretory vesicles (Fremeau, Kam et al. 2004; Takamori 2006).

The "dying forward" hypothesis of ALS etiology posits that motor neuron degeneration is the result of cortical cell hyperexcitability, which induces modifications of glutamatergic activity in upper motor neurons. This cascade subsequently promotes anterior horn cell degeneration through an anterograde transsynaptic diffusion of excitotoxicity (Maekawa et al. 2004; Vucic et al. 2011). Consistent with this hypothesis, transcranial magnetic stimulation studies have established that cortical hyperexcitability is an early feature of sALS and even precedes the clinical onset of fALS (Vucic et al. 2008). Remarkably, presymptomatic upper motor neuron hyperexcitability has been reported in G93A mice that model fALS and in wobbler mice that model sALS (Stys 2005; Pieri et al. 2009; Carunchio et al. 2010; Nieto-Gonzalez et al. 2010). "Whether neuronal hyperexcitability is associated with the cell alterations" and abnormal glutamate concentration recognized as the cause of neuronal injury (Shobha et al. 2007; Bogaert et al. 2010; Foran et al. 2011) remains unknown. Here, we showed that motor cortex from 1-month-old G93A mice exhibit hyperexcitability associated with neuronal morphological changes and with abnormalities in glutamate packaging that favor glutamate accumulation in the synaptic terminals surrounding hyperexcitable neurons.

Materials and Methods

Animals

The experiments were performed using B6SJL-TgN (SOD1)2 Gur mice that overexpressed wild-type human SOD1 (SOD1), B6SJL-TgN (SOD1-G93A)1 Gur mice that over-overexpressed the G93A-mutated human SOD1 (G93A) constructed by Gurney (1994), and non-transgenic littermates as the control. The mice were originally obtained from Jackson Laboratories (Bar Harbor) and then housed in our animal facilities. On postnatal day 21, the animals were weaned, and a screening for the presence of the human transgene was performed on the tail tips as previously described (Beauchamp and Fridovich 1971; Pieri et al. 2003). The mice carrying the transgene G93A, but not SOD1 or control mice, showed signs of hind limb weakness and rapidly developed a paralysis that resembled fALS both clinically and pathologically (Gurney 1994) at 4 months of age and died within 7–14 days.

Procedures involving the animals and their care were conducted in strict accordance with the Policy on Ethics approved by the Society for Neuroscience and with the European Communities Council Directive of 24 November 1986 (86/609/EEC) regarding the care and use of animals for experimental procedures. All experiments were approved by the Animal Welfare Committee of the Italian Ministry of Health and the Regional Animal Ethics Committee. Every effort was made to minimize the number of animals used and their suffering.

Slice Preparation

control, G93A, and SOD1 male mice, aged 26 postnatal days (P26) to P31, were anesthetized with halothane (Sigma–Aldrich) and decapitated. The brains were removed and placed in cold artificial cerebrospinal fluid solution (ACSF) containing the following (in mM): 126 NaCl, 26 $NaHCO_3$, 2.5 KCl, 1.25 NaH_2PO_4, 2 $MgSO_4$, 2 $CaCl_2$, and 10 glucose, gassed with 95% O_2–5% CO_2 (pH 7.4, 300 mOsm). Coronal slices (275 μm) were obtained as previously described (Carunchio et al. 2010) using a vibratome (Leica VT1000S), covering approximately from 1.18 mm anterior to the bregma (anteriorly) to –0.34 mm posterior to the bregma. Slices were then incubated in the oxygenated ACSF, initially at 37°C for 45 min and subsequently at room temperature (RT). The single slice was then transferred to a recording chamber and submerged in continuously flowing oxygenated ACSF (31°C, 2 mL/min) for electrophysiological experiments. Some slices were utilized for biochemical, molecular, and immunohistochemical experiments.

Electrophysiology

Recordings were obtained from the deep part of Layer V pyramidal neurons of the primary motor cortex (M1), which were visually identified by their typical large soma size and the presence of a thick apical dendrite oriented toward the pial surface (Stuart et al. 1993) using an upright infrared microscope (Axioskop 2 FS), a 40× water immersion objective (Achroplan), and a CCD camera (Cool Snap, Photometrics). Only neurons with a typical pyramidal-shaped soma, regular-spiking, a membrane resistance lower than 100 MΩ, and a membrane capacitance in the range of 75–125 pF, corresponding to a diameter of 16–21 μm for all experimental groups (Oswald et al. 2013; Suter et al. 2013), were considered in this study. Neurons with electrophysiological properties different from those typical of cortico-spinal motor neurons have been rejected.

For the electrophysiological whole-cell recordings, borosilicate glass pipettes (outside diameter 1.5 mm; tip resistance 3–4 MΩ) were used. In order to morphologically identify the recorded cells, some neurons were filled with 2% biocytin (Sigma–Aldrich) through the recording pipette.

The passive membrane properties and the pattern of repetitive firing were examined in the cortical motor neurons using a current-clamp configuration. The pipettes were filled with an intracellular solution containing (in mM): 145 KGlu, 1 EGTA, 0.1 $CaCl_2$, 10 HEPES, 2 $MgCl_2$ and 2 Mg-ATP (pH 7.3, 300 mOsm). The resting membrane potential was measured immediately after establishing the whole-cell recording configuration. Various intensities of hyperpolarizing rectangular current pulses of 500-ms

duration were used to determine the basic electrophysiological properties. The membrane resistance of the cell was calculated as the slope of the linear fit to the *I–V* relationship for currents between –60/+40 pA. The time constant of the membrane (τ membrane) was calculated on the membrane potential variation in response to a –100 pA hyperpolarizing current, fitted to the single exponential function:

$$V_m = V_r + (V_f - V_r)(1 - e^{t/\tau}),$$

where V_m is the membrane potential, V_r is the resting membrane potential, V_f is the final value of the membrane potential, t is the time, and τ is the membrane time constant.

The action potential (AP) firing was recorded using 1-s depolarizing current steps (+20/+100-pA, 20-pA steps). For each neuron, the firing frequency was plotted against the injected currents (F–I relationship), and the gain value was calculated as the slope of the linear fitting.

Rheobase is a measure of membrane excitability and was calculated as the horizontal asymptote of the hyperbolic curve obtained by fitting the injected current values, which were delivered at different durations (2 pA increments at 100–200–300–500–800 ms), that were required to evoke an AP for each recorded neuron. The points were fitted with the general hyperbolic equation:

$$y = P_1 x/P_2 + x,$$

where P_1 represents the horizontal asymptote.

Spontaneous excitatory postsynaptic currents (sEPSCs) were recorded in a voltage-clamp configuration (–70 mV holding potential) using electrodes filled with an intracellular solution containing (in mM): 139.5 cesium methanesulfonate ($CsMeSO_3$), 1 ethylene glycol bis (β-aminoethyl ether)-*N*,*N*,*N*′,*N*′-tetraacetic acid (EGTA), 5.5 $CsCl_2$, 0.1 $CaCl_2$, 10 *N*-2-hydroxyethylpiperazine-*N*′-2-ethanesulfonic acid (HEPES), 2 $MgCl_2$, and 2 Mg-ATP (pH 7.3, 300 mOsm). By using ACSF and this internal solution, the chloride equilibrium potential, which was calculated by the Nernst equation, was –70 mV. Under these experimental conditions, the net flux of chloride ions was null, which ensured that only glutamatergic excitatory currents were recorded. Furthermore, at the holding potential of –70 mV and using ACSF containing $MgCl_2$, the sEPSCs mediated by NMDA receptors were nullified. In some experiments, the AMPA/Kainate antagonist 6-cyano-7-nitroquinoxyline-2,3-dione (CNQX, 10 μM) was added to the ACSF. In this condition, all synaptic events were blocked, which indicated that they were due to the activation of AMPA/Kainate receptors. In some experiments, the voltage-gated sodium channel blocker tetrodotoxin (TTX 1 μM, Sigma–Aldrich) was added to the ACSF in order to record quantal miniature excitatory postsynaptic currents (mEPSCs).

After the formation of a high-resistance seal (>1 GΩ), the capacitance and the resistance of the electrodes were compensated electronically. The signals were amplified using a Multiclamp 700B patch-clamp amplifier (Molecular Devices), sampled at 20 KHz, filtered at 3 KHz, and stored in a computer. The data were acquired with a Digidata 1400A (Molecular Devices). The capacitance and resistance membrane values were obtained using the Membrane test function of pClamp 10 software (Molecular Devices). Whole-cell access resistances measured in the voltage-clamp mode were in the range of 5–20 MΩ.

Cell Labelling of Recorded Cells

Immediately after recording, the slices containing biocytin-loaded cells were fixed by immersion in 4% paraformaldehyde in 0.1 M PBS overnight at 4°C. The slices were collected in PBS, rinsed 3 times in the same buffer, and then incubated with Cy2-conjugated Streptavidin (1 : 200; Jackson Immunoresearch Laboratories) in PBS 0.3% Triton X-100 for 3 h at RT.

After three 5-min washes in PBS, the slices were incubated overnight at 4°C in PBS containing 1% bovine serum albumin, 1% Triton X-100, and the following primary antibodies: rabbit anti-VGluT1 (1 : 1000; Synaptic System) and mouse anti-VGluT2 (1 : 1000; Millipore). The slices were then washed 3 times in PBS and incubated for 2 h at RT with a cocktail of secondary antibodies, including Alexa Fluor 555 donkey anti-rabbit IgG and Alexa Fluor 647 donkey anti-mouse IgG (Invitrogen). Furthermore, to assess the cytoarchitectonic areas and layers of the different recorded slices, the latter were counterstained with NeuroTrace® 640⁄660 deep-red Fluorescent Nissl Stain (Invitrogen). After additional 3 washes in PBS, the sections were mounted using an anti-fade medium (Fluoromount; Sigma).

Neurons of interest were identified on 10× objective (Plan-Apochromat, Zeiss; NA = 0.30) and captured on 40× oil immersion objective (NA = 1.3; zoom factor 0.5) through a confocal laser-scanning microscope (CLSM700; Zeiss). The following acquisition settings were used: image format 1024 × 1024; image size 318.8 × 319.8 μm; Airy units 1.55 producing an optical section thickness of 1.2 μm; 25 z-stack series with az-spacing 1.25 μm; pixel dwell time 3.15 μs. To generate projection images, the maximum intensity algorithm of the CLSM software was used. The confocal image acquisitions were performed so that all samples were captured using consistent settings for laser power and detector gain.

Although confocal imaging is an indispensable tool for analysis of neural components at the subcellular and cellular level of organization, using thick slices of 275-μm confocal imaging has some limitations that must be taken into account. In these very thick slices, photobleaching of the fluorophores in focal planes can be problematic and the collection of a stack of images from such an extended volume can degrade the signal from deeper sections compared with those from the surface. In our study, in order to reduce photobleaching, we used a low number of scans (maximum 4) and a low laser power (maximum 7%). Furthermore, to generate the projection image, the first and the last images of the z-series were discarded, so that only central images were used. These procedures allowed a better image definition and a more reliable analysis. Finally, the figures were generated by adjusting only the brightness and the contrast and were composed using Adobe Illustrator CS5.

Histology and Immunohistochemistry

The animals were perfused transcardially with 50 mL of saline, followed by 50 mL of 4% paraformaldehyde under anesthesia, which was induced by intraperitoneal injections of Rompun (xylazine, 20 mg/mL, 0.5 mL/kg body weight) and Zoletil (tiletamine and zolazepam, 100 mg/mL and 0.5 mL/kg body weight). Each brain was removed immediately, post-fixed in the same paraformaldehyde solution for 2 h, and after 3 washes in PBS, it was transferred to a 30% sucrose solution at 4°C until it sank. The brains were cut into 6 series of 30-μm-thick transverse sections using a freezing microtome, and the slices were collected in PBS. Furthermore, the sections were incubated overnight at 4°C in PBS containing 0.3% Triton X-100, the following primary antibodies: rabbit anti-VGluT1 (1 : 1000; Synaptic System), guinea pig

anti-VGluT2 (1 : 1000; Millipore), and mouse anti-SMI32 (1 : 1000; Covance), and 1% bovine serum albumin to block the unspecific binding of the antibodies. After 3 washes in PBS, the sections were incubated for 2 h at RT with a cocktail of secondary antibodies, including Alexa Fluor 555 donkey anti-guinea pig IgG, Alexa Fluor 405 donkey anti-rabbit IgG, and Alexa Fluor 488 donkey anti-mouse IgG (1 : 200; Invitrogen).

Furthermore, the sections were counterstained with NeuroTrace® 640/660 deep-red Fluorescent Nissl Stain (1 : 200; Invitrogen). After further washes in PBS, the sections were mounted using an anti-fade medium (Fluoromount; Sigma) and examined under a confocal laser-scanning microscope (Zeiss CLSM700).

The specificity of immunohistochemical labeling was confirmed by the omission of primary antibodies and the use of normal serum instead (negative controls).

The cytoarchitectonic areas and layers of the different slices were further determined in Nissl-stained sections according to Franklin and Paxinos' Atlas of Mouse Brain (Franklin and Paxinos 1997) and to Zilles (Zilles 1985). The M1 was defined anteriorly from 1.18 mm to the bregma to posteriorly –0.34 mm to the bregma, as defined by Franklin and Paxinos (1997).

The relatively narrow Layer IV and thick Layer V defined the lateral and medial boundaries of M1, and ventral boundaries consisted of the most dorsal part of the corpus callosum as previously described (Oswald et al. 2013).

The area of interest (M1) was identified by using a 10× objective (Plan-Apochromat, Zeiss; NA = 0.30; zoom factor 0.5) and captured through a confocal laser-scanning microscope (CLSM700; Zeiss). The following acquisition settings were used: image format 1024 × 1024; image size 1279.1 × 1279.1 μm; Airy Units 1.37 producing an optical section thickness of 13.2 μm; pixel dwell time 12.61 μs. The confocal image acquisitions were performed so that all samples were captured using consistent settings for laser power and detector gain. Finally, the figures were generated by adjusting only the brightness and the contrast and were composed using Adobe Illustrator CS5.

Morphological Analysis

Measurements of dendrite arborization were performed in previously recorded neurons (cell = 16 per group; $N = 4$ per group) filled with biocytin. Given that the thickness of slices (275 μm) imposed by electrophysiological recordings prevented visualization of the entire dendritic arborization of neurons, the analysis was restricted to the basal dendrite compartment which, having a reduced extension, presented only few truncated dendrites. First, the total length of basal dendrites was measured using an optical microscope (DMLB, Leica) equipped with a motorized stage and a camera connected to software (Neurolucida 7.5, MicroBrightField) that allowed a quantitative 3D analysis of the entire compartment. Then, following the application of a grid with concentric circles (distance between circles: 25 μm) on the screen of the monitor, both the length of the dendrite portions within each ring and the number of intersections with each circle were measured at an increasing radial distance from the center of the soma (Sholl analysis) using Neurolucida Explorer software.

Additional groups of previously recorded biocytin-filled neurons (cell = 11 per group; $N = 4$ per group) were used for spine density measurements carried out using a Zeiss CLSM700 confocal laser-scanning microscope (Zeiss). Neurons of interest were identified on 10× objective, and spines were captured with a 63× oil immersion objective (Plan-Apochromat, Zeiss; NA = 1.4) zoom factor 2.0; image format was 1024 × 1024; image size was 50.8 × 50.8 μm; Airy Units 1 producing an optical section thickness of 1.3 μm; z-spacing 0.20 μm; number of optical sections was about 70–80; pixel dwell time 0.79 μs. For each neuron, three to five 30–100-μm dendritic segments were randomly acquired for spine counts. After image collection, each segment was analyzed for spine density using the Imaris 7.6.5 (Bitplane AG) software. Only protrusions with a clear connection of the head of the spine to the dendrite shaft were counted as spines. Spine density was then expressed as the number of spines per 10-μm dendrite length. The experimenters were blind to the experimental group.

Densitometric Analysis of Fluorescence Images

Densitometric analysis of the target proteins, namely VGluT1 and VGluT2, was performed on perfused mouse brain sections.

In order to avoid staining variability among sections and experimental groups, sections of mouse brains were incubated with the same cocktail of primary and secondary antibodies at the same time. Furthermore, confocal settings (described earlier) for image capture were maintained constant throughout the acquisition of sections from the 3 groups of mice. After confocal acquisition (described earlier), images were exported in TIFF and analyzed with ImageJ software (http://rsb. info.nih.gov/ij/; National Institutes of Health).

The background signal for all antibodies was determined in a non-stained area. For each channel, the threshold was adjusted according to the background signal and kept constant between sections. VGluT1- and VGluT2-associated signals were quantified in the layers of interest by manually outlining individual layers (Layer II/III and V) through overimposing fluorescent Nissl staining on the VGluT1 or VGluT2 signals. For Layer II/III and Layer V (deep part), mean signal intensities (F) of VGluT1 and VGluT2 were performed on 2 squared frames (100 μm per side) pseudo-randomly distributed medio-laterally on the 6 sections, one every 250 μm, sampled in every mouse to cover the M1 rostro-caudal extent entirely. The F/A ratio defines mean fluorescence of individual samples (F) normalized to total cellular surface (A). Accordingly, quantification was done on 12 samples per mouse (5 mice per group—total group samples $n = 60$). Data collecting for densitometry was done by experimenter blind to the group analyzed.

Tissue Lysate Preparation and Western Blot Analyses

Motor cortex (M1) was isolated under a dissection microscope using the cingulum, the ventricles, and the corpus callosum as landmarks from 275-μm-thick coronal slices, prepared as described earlier. Slices were placed on a 0.5-mm square grid, the medial cut was performed on the vertical of the cingulum, and the lateral cut was approximately 1 mm. Ventral cut followed the border with the callosum. Afterward, the isolated portion of M1 was homogenized, and the proteins were extracted in RIPA buffer (50 mM NaCl, 50 mM Tris–HCl pH 7.4, 10% glycerol, 320 mM sucrose, 1% TX100, plus protease inhibitor cocktail, 1 mM Na_3VO_4, 1 mM DTT, and 5 mM NaF) for 30 min on ice and then were centrifuged for 10 min at 4°C (14.000 rpm). The supernatants were collected, and the protein content was quantified by Bradford's colorimetric assay (Bio-Rad). Each protein sample was separated by SDS–polyacrylamide gel electrophoresis and transferred to a nitrocellulose membrane. The membranes were saturated with 5% dried nonfat milk and incubated overnight with specific primary antibodies, including rabbit anti-VGluT1 (1 : 10 000; Synaptic System), rabbit anti-VGluT2 (1 : 10 000; Synaptic System), and mouse anti-β-actin (1 : 5000; Sigma).

The membranes were then incubated with the appropriate horseradish peroxidase-conjugated secondary antibodies. Immunoreactive bands were detected using an enhanced chemiluminescence kit (ECL; Amersham Biosciences). The relative levels of immunoreactivity were determined by densitometry using the software ImageQuant 5.0. Samples were incubated with the specific primary antibodies. Densities of protein bands in the western blots were measured, and mean ratios between proteins and β-actin were reported as percentage of control values.

Quantitative Real-Time PCR

The M1 was isolated from coronal slices as described earlier. RNA was extracted using TRIzol reagent (Invitrogen). Any remaining genomic DNA was eliminated with an RNase-Free DNase Set (Qiagen) according to the manufacturer's instructions. 1 µg of total RNA was used for the RT reaction using the SuperScript VILOTM cDNA Synthesis Kit (Invitrogen). The following real-time PCR (RT-PCR) program was used: 25°C for 10 min, 42°C for 60 min, and 85°C for 5 min. The expression of the different primers was assessed by quantitative RT-PCR (qRT-PCR) using a SensiMixTM SYBR Kit (Bioline) as a fluorescent dye to monitor cDNA amplification. The following PCR program was used: 95°C for 10 min, 40 cycles at 95°C for 5 s, and 60°C for 100 s. The primers used included mouse VGluT1 F (5′-TTTGAGATCAGCAAGGTGGGG-3′), mouse VGluT1 R (5′-GTGACGACTGCGCAAAAAGT-3′), mouse VGluT2 F (5′-ATCATTGTGCCTATCGGGGG-3′), mouse VGluT2 R (5′-GCCAAAACCCCCACAATTCA-3′), mouse β-actin F (5′-GCTCC GGCATGTGCAAAG-3′), and mouse β-actin R (5′-CCATCACACCCTG GTGCCTA-3′). β-Actin was used as the housekeeping gene for quantity normalization. 1 µl of the first strand of cDNA product was used for amplification (in triplicate) in 20 µL reaction solution, which contained 10 µL of iQTM SYBR Green Supermix (Bio-Rad) and 1 µmol of each primer. The following PCR program was used: 95°C for 3 min, 40 amplification cycles at 95°C for 10 s, 56°C for 20 s, and 72°C for 30 s. The fold-change was determined by the $2^{-\Delta\Delta CT}$ method.

Statistical Analyses

The analysis of current-clamp recordings was performed off-line using the software Clampfit 9 (Molecular Devices). The data are presented as the mean ± standard error (SE), with "*n*" indicating the number of analyzed neurons and "N" the number of used animals. Statistically significant differences were determined using the one-way ANOVA test followed by Bonferroni's post hoc test and the unpaired Student's *t*-test, when necessary. To analyze synaptic activity, the 6.0.7 version of Mini Analysis Program (Synaptosoft, Inc.) was used. sEPSCs and mEPSCs were manually detected using a 10 pA threshold crossing algorithm. The interevent interval (IEI), the event amplitude, the area, and the kinetic parameters (rise and decay times) were compared between the control, G93A, and SOD1 mice. The cumulative amplitude and IEI plots obtained from a single cell in the different neuronal groups were compared using the Kolmogorov–Smirnov (K–S) test. Statistical analysis was performed using Origin 7 (Microcal Software) and SPSS 17.0 for Windows (SPSS, Inc.) software. Differences in total dendrite length were estimated using the statistical Student's *t*-test. Differences in dendrite length and branch nodes at increasing distance from the soma were estimated using two-way ANOVAs with "genotype" as main factor and "radial distance from soma" as repeated factor. Students *t* tests were used for post hoc comparisons of groups at specific segments, and for between-group comparisons of spine density. Values of $P < 0.05$ were considered statistically significant.

Results

Morphological Reconstruction of Layer V Cortical Pyramidal Motor Neurons by Biocytin Labelling

To validate the neuronal type identified by infrared illumination, a subset of putative Layer V pyramidal neurons that were characterized by the typical repetitive firing of cortico-spinal neurons ($n = 40$; control $n = 18$; G93A $n = 18$; SOD1 $n = 4$), localized in the M1 of the coronal slices, was filled with biocytin to reveal their morphological features. All recorded neurons filled with biocytin in fluorescent Nissl-stained slices were located in the deep portion of Layer V of the M1 area (Fig. 1A). Furthermore, all recorded biocytin-labeled neurons presented classical features of spiny pyramidal neurons. Specifically, they displayed a triangular-shaped soma, a large apical dendrite, and multiple basal dendrites (Fig. 1A′).

G93A Layer V Corticomotor Neurons Show Paroxysmal Hyperexcitability

The single motor neuron excitability was analyzed by performing whole-cell patch-clamp recordings, in current-clamp mode, in P26–P31 control, SOD1, and G93A mice. Only neurons that looked like pyramidal and that responded to a current injection with repetitive firing, as reported in Materials and Methods, were considered for the final analysis. Because there were no significant differences between control and SOD1 in all the experiments reported in this study, the 2 experimental groups were unified and denoted as control.

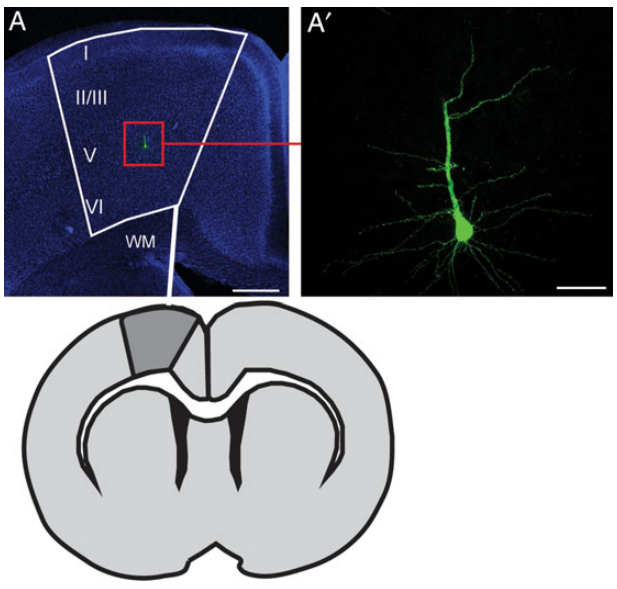

Figure 1. Localization of Layer V pyramidal neurons in the mouse M1. (*A*) Schematic and low-magnification pictures showing the localization of recorded and then biocytin-filled neurons (red square) in a 275-µm coronal section Nissl-counterstained in the motor cortex (M1) delimited by white lines. (*A′*) Confocal microscope image of a biocytin-loaded pyramidal neuron recorded from a mouse coronal slice. Note the triangular shape of the soma, the large apical dendrite, and the multiple basal dendrites typical of the pyramidal neurons of the cerebral cortex. Scale bars in Panel *A*: 400 µm; in Panel *A′*: 50 µm. WM = white matter; I–VI = cortical layers.

The membrane passive properties were analyzed in the control ($N = 8$) and G93A ($N = 8$) pyramidal neurons. The injection of currents (500 ms) of different amplitudes from the resting membrane potential, which evoked responses that reached a steady-state of potentials, was used to calculate the membrane's passive properties. In particular, the resting membrane potential (control: −64.26 ± 0.94 mV, $n = 31$; G93A: -65.99 ± 1.02 mV, $n = 17$; $P > 0.05$ unpaired Student's t-test), the membrane resistance (control: 144.27 ± 11.82 MΩ, $n = 31$; G93A: 182.34 ± 17.16 MΩ, $n = 17$; $P > 0.05$ unpaired Student's t-test), and the τ membrane (control: 19.75 ± 1.21 ms, $n = 31$; G93A: 23.68 ± 2.68 ms, $n = 17$; $P > 0.05$ unpaired Student's t-test) were unaffected by mutated human transgene overexpression (data not shown).

To analyze the neuronal intrinsic excitability, the *F–I* gain values were calculated, as described in Materials and Methods. The AP firings in response to 1-s depolarizing current steps (+20/+100-pA, 20-pA steps) were recorded under the current-clamp condition in the control and G93A motor neurons and, for all injected currents equal to or above +40 pA, the firing frequency in the G93A neurons was significantly higher compared with the control neurons (Fig. 2*A*), confirming previously reported results (Carunchio et al. 2010). The gain values, calculated for each neuron, were significantly higher in the G93A neurons (0.15 ± 0.01, $n = 17$) than the control neurons (0.10 ± 0.01, $n = 31$; $P < 0.01$ unpaired Student's t-test; Fig. 2*B*,*C*).

Finally, the rheobase parameter was calculated as described in Materials and Methods. In the G93A motor neurons, the current amplitude required to evoke an AP was lower compared with the control neurons (control: 70.20 ± 5.02 pA, $n = 31$; G93A: 47.24 ± 6.10 pA, $n = 17$; $P < 0.01$ unpaired Student's t-test; Fig. 3), which confirmed the higher excitability in neurons expressing mutant SOD1.

G93A Layer V Corticomotor Neurons Show Increased Frequencies of Spontaneous and Miniature Excitatory Postsynaptic Currents

To verify the status of excitatory neurotransmission in the G93A motor neurons, firstly sEPSCs were recorded in acutely prepared cortical slices from the P26–P31 control ($N = 7$) and G93A ($N = 6$) mice. Layer V pyramidal neurons in the M1 region receive intercortical excitatory inputs from higher layers (Layer II/III) at the level of their apical dendrites and intracortical excitatory inputs at the level of their multiple basal dendrites (Hooks et al. 2013; Petersen and Crochet 2013; Shepherd 2013). In this work, whole-cell voltage-clamp recordings were carried out ($V_{hold} = -70$ mV) from Layer V cortical pyramidal neurons using $CsMeSO_3$-filled patch-pipettes. In these experimental conditions, only spontaneous synaptic currents mediated by AMPA/Kainate receptors were recorded (see Materials and Methods) in the control and G93A neurons. The sEPSCs were completely abolished when CNQX (10 μM) was added to the ACSF, which confirmed that the synaptic events were mediated by non-NMDA receptors (Fig. 4*A*).

The analysis of the sEPSCs demonstrated that the mean of the IEIs was significantly shorter in the G93A compared with the control (Fig. 4*B*), which indicated that the G93A motor neurons were characterized by an increased frequency of the sEPSCs compared with the control (control: 4.52 ± 0.59 Hz, $n = 31$; G93A: 8.21 ± 1 Hz, $n = 21$; $P < 0.01$, unpaired Student's t-test; Fig. 4*C*). The mean amplitude of the sEPSCs was not significantly different between the 2 neuronal groups ($P > 0.05$, unpaired Student's t-test; Fig. 4*D*,*E*). Furthermore, the analyses of the current kinetics showed that the rise time (control: 1.96 ± 0.075 ms, $n = 31$; G93A: 1.95 ± 0.057 ms, $n = 21$), the decay time (control: 7.79 ± 0.37 ms, $n = 31$; G93A: 7.39 ± 0.38 ms, $n = 21$), and the area of sEPSCs (control: 84.90 ± 7.58 pA × ms, $n = 31$; G93A: 93.03 ± 8.99 pA × ms, $n = 21$) were not different between the G93A and control neurons ($P > 0.05$, unpaired Student's t-test; data not shown).

In order to block AP-dependent neurotransmitter release and to verify whether a general cortical environment alteration occurs, we performed whole-cell recordings of quantal miniature glutamate events (mEPSCs) in Layer V pyramidal neurons by adding TTX (1 μM) in the bath (Fig. 5). As well as sEPSCs, a higher frequency of the mEPSCs was observed in G93A (3.12 ± 0.35 Hz, $n = 22$, $N = 9$; $P < 0.01$, unpaired Student's t-test; Fig. 5*B*) than that in control motor neurons (1.78 ± 0.24 Hz, $n = 24$, $N = 11$), whereas no difference was observed for the events amplitude ($P > 0.05$, unpaired Student's t-test; Fig. 5*C*), decay time (control: 7.06 ± 0.29 ms, $n = 24$, $N = 11$; G93A: 6.05 ± 0.22 ms, $n = 22$, $N = 9$; $P > 0.05$, unpaired Student's t-test), and rise time (control: 1.78 ± 0.08 ms, $n = 24$, $N = 11$; G93A: 1.64 ± 0.05 ms, $n = 22$, $N = 9$; $P > 0.05$, unpaired Student's t-test, data not shown).

G93A Layer V Hyperexcitable Corticomotor Neurons Show Expanded Dendrite Arborisation without Variations in the Spine Density

There is evidence that the formation of dendritic arbors is an activity-dependent regulated process with size and geometry being adjusted as a function of the level and the distribution of inputs received (Tripodi et al. 2008). Thus, the augmentation of single-cell discharge and EPSC frequency in the G93A mice Layer V motor neurons might strongly affect the dimension and ramification of the dendritic arbor in these same neurons. To examine this point, previously recorded biocytin-filled neurons from G93A mice and control mice were compared for the extent of their basal dendrite arborization and the density of spines in the same dendrite compartment. Results first revealed that basal dendrites in G93A Layer V motor neurons were globally longer ($P < 0.01$, Fig. 6*A*–*C*) compared with the control neurons. Sholl analysis data then revealed that G93A dendrites were longer (Fig. 6*D*) and exhibited more intersections with the concentric circles (Fig. 6*E*) compared with the control dendrites at distances ranging between 50 and 125 μm from the center of the soma (dendritic length: 50 μm $P < 0.05$, 100 μm $P < 0.01$, 125 μm $P < 0.05$; intersections: 50 μm $P < 0.05$, 75 μm $P < 0.05$, 100 μm $P < 0.05$). However, the spine density calculated on basal dendrites was not found to vary between G93A and control mice ($P > 0.05$; Student's t test; Fig. 6*F*–*H*).

Vesicular Glutamate Transporter 2 (VGluT2) mRNA and Protein Levels are Increased in Synaptic Terminals Surrounding G93A Layer V Corticomotor Neurons

We then investigated whether the increased frequency of EPSCs observed in the M1 of G93A mice was influenced by an increase of glutamate-containing vesicles at the presynaptic level (Moechars et al. 2006). We investigated the expression level of 2 VGluTs, namely, the vesicular glutamate transporter 1 (VGluT1) and the vesicular glutamate transporter 2 (VGluT2), in the control and G93A mice. In the M1, where Layer IV is almost absent, in both the control and G93A mice, all layers showed a diffused VGluT1 immunoreactivity (Fig. 7*A*–*H*). Densitometric analysis of VGluT1 immunoreactivity (IR) in M1 cortical layers showed that, in Layer II/III of G93A (F/A = 0.37 ± 0.015), VGluT1 IR was not significantly different compared with control (F/A = 0.36 ± 0.016; $P > 0.05$ paired Student's t-test). Similarly, in the deep part of Layer V of

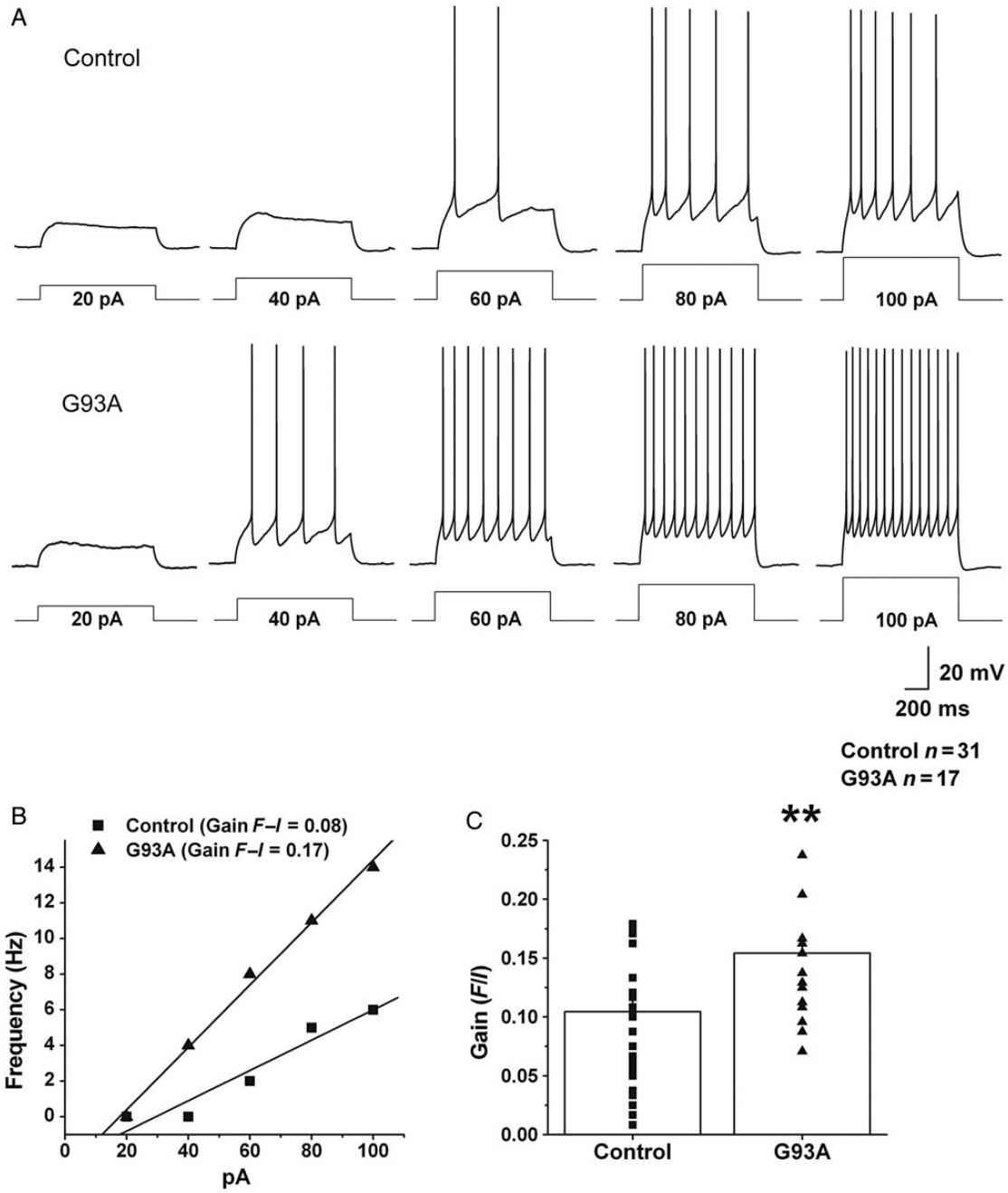

Figure 2. Neuronal hyperexcitability is a feature of G93A cortical motor neurons. (*A*) Representative repetitive firing in control and G93A neurons evoked by +20, +40, +60, +80 and +100 pA current injections (1 s) under the current-clamp condition. The number of APs evoked by the same injected current was higher in the G93A motor neurons compared with the control. (*B*) AP frequencies plotted against the injected current intensities of the representative control and G93A neurons shown in *A*. The points were fitted with straight lines, and the slopes represent the gain (*F–I*) values. (*C*) Bar plot of the means ± standard errors of the gains in the control (0.10 ± 0.01, $n = 31$, $N = 8$) and G93A (0.15 ± 0.01, $n = 17$, $N = 8$) neurons. **$P < 0.01$ unpaired Student's *t*-test.

G93A mice (F/A = 0.38 ± 0.018), VGluT1 IR was not significantly different to control (F/A = 0.36 ± 0.017; $P > 0.05$ paired Student's *t*-test; data not shown).

Conversely, VGluT2 immunoreactivity in the different layers of M1 was significantly different between the control and G93A mice (Fig. 8*A–H*). In the control mice, only the deep part of Layer II/III showed a weak VGluT2 immunoreactivity (Fig. 8*A–D*). In the G93A mice, VGluT2 immunoreactivity in the M1 was more intense compared with the control (Fig. 8*A–H*). Specifically, in the G93A, we found that the deep part of Layer II/III showed a clear and intense VGluT2 immunoreactivity (Fige 8*E*). Furthermore, in the G93A mice, a moderate VGluT2 immunoreactivity, which was not present in the control (Fig. 8*A*), was observed in the deeper part of Layer V (Fig. 8*E*). Densitometric analysis of VGluT2 immunoreactivity (IR) in M1 cortical layers showed that, in Layer II/III of G93A (F/A = 0.32 ± 0.015), VGluT2 IR was significantly higher compared with control (F/A = 0.22 ± 0.016; $P < 0.0001$ paired Student's *t*-test). Similarly, in the deep part of Layer V of G93A mice (F/A = 0.30 ± 0.016), VGluT2 IR was significantly higher than that in control (F/A = 0.12 ± 0.008; $P < 0.0001$ paired Student's

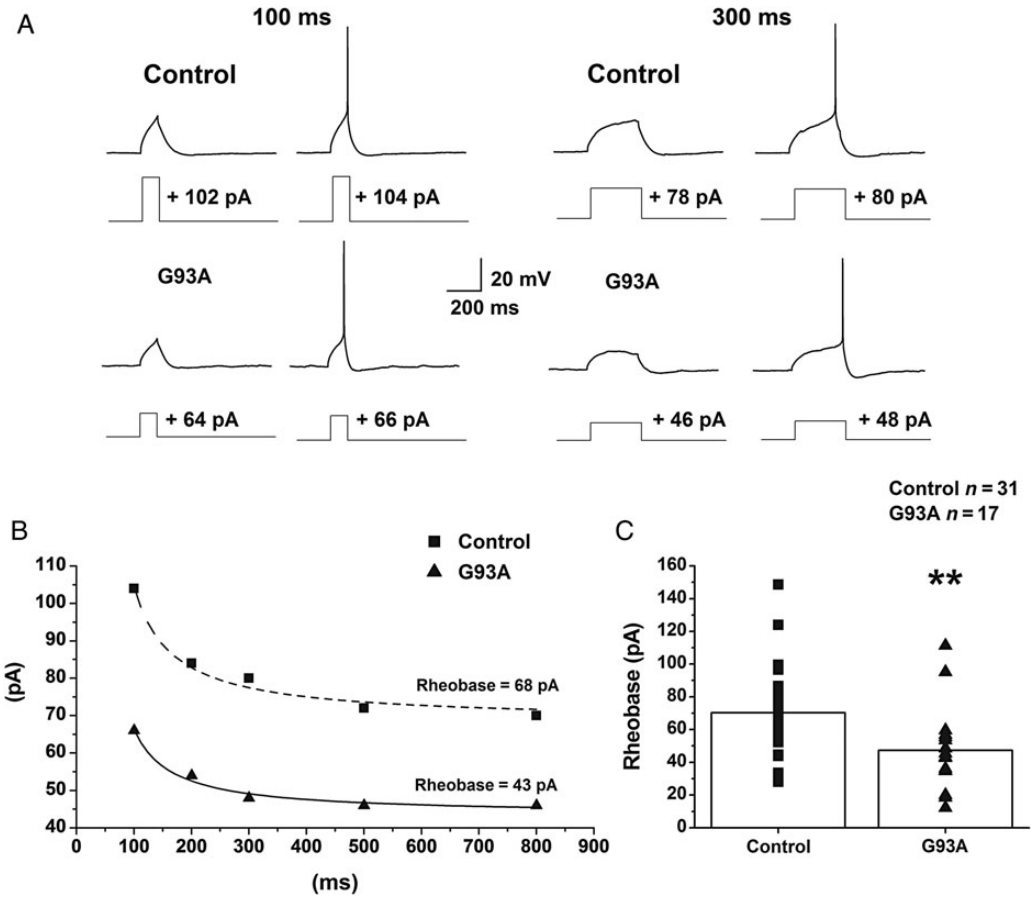

Figure 3. The rheobase in G93A was significantly lower compared with the control motor neurons. (*A*) Representative traces of current injections (100 and 300 ms) required to evoke an AP in representative control and G93A neurons. (*B*) Hyperbolic curves obtained by fitting the amplitude of the injected currents required to evoke an AP, plotted against the duration of the electrical stimulations. (*C*) Bar plot of the means ± standard errors of the rheobase values in the control (70.20 ± 5.02 pA, $n = 31$, $N = 8$) and G93A (47.24 ± 6.10 pA, $n = 17$, $N = 8$) neurons. $^{**}P < 0.01$ unpaired Student's *t*-test.

t-test; data not shown). As expected, because of the higher density of VGluT2 in the presence of a stable density of VGluT1, we observed a decreased VGluT1:VGluT2 ratio of G93A mice compared with control in both Layers II/III (1.15 vs. 1.63) and V (1.26 vs. 3.0).

To confirm that changes in VGluT2 IR were confined to M1 and did not affect other cortical areas, we analyzed VGluT2 expression in the primary somatosensory cortex (S1) of G93A and control mice. Qualitative and quantitative observations showed that, in S1, no differences in VGluT2 IR were present between G93A and control mice (Supplementary Fig. 1). Densitometric quantification was done on $n = 50$ samples per group (control $N = 5$; G93A $N = 5$).

To better define the distribution of the VGluT1- and VGluT2-synaptic terminals surrounding Layer V pyramidal neurons, we performed VGluT1- and VGluT2 immunofluorescence on the slices of the control and G93A mice that contained the biocytin-filled neurons (Fig. 9*A*–*D*).

We found that, in the control mice, the synaptic terminals located over the biocytin-filled pyramidal cells of Layer V predominantly expressed VGluT1 (Fig. 9A), whereas only a few synaptic terminals expressed VGluT2 (Fig. 9B). In the G93A mice, we observed many more synaptic contacts on the biocytin-filled pyramidal cell of Layer V compared with the control and an almost equal representation of VGluT1 and VGluT2 terminals (Fig. 9*C*,*D*).

Furthermore, to additionally confirm the data on VGluTs, we performed qRT-PCR ($N = 7$ per group) and western blotting on the M1 in the G93A and control mice ($N = 6$ per group). qRT-PCR results confirmed the immunohistochemical data. VGluT1 mRNA levels were similar in the G93A and control mice ($P > 0.05$, paired Student's *t*-test; Fig. 9*E*). VGluT2 mRNA levels differed significantly in the G93A compared with the control mice, with the former presenting more than a 2-fold increment ($P < 0.01$, paired Student's *t*-test; Fig. 9*E*). Similarly, the western blot analysis showed no significant differences in the VGluT1 expression level between the G93A and control ($P > 0.05$, paired Student's *t*-test; Fig. 9*F*), but a large increase in the level of VGluT2 protein ($P < 0.01$, paired Student's *t*-test; Fig. 9*F*) in the G93A compared with the control. These results demonstrate that VGluT2 expression, as detected by immunohistochemistry, qRT-PCR, and western blotting, was significantly higher in the G93A than that in control mice.

Discussion

This study provides evidence of alterations in the functional and structural properties of G93A corticomotor neurons and an abnormal glutamatergic activity in their immediate environment. The functional alterations consisted of significantly lower rheobase values of single motor neurons, associated with a frequency augmentation of the sEPSCs and mEPSCs. In ALS patients, a lower rheobase value of motor axons has already been observed (Mogyoros et al. 1996; Mogyoros et al. 1998). Neuronal hyperexcitability has been previously reported in different central nervous

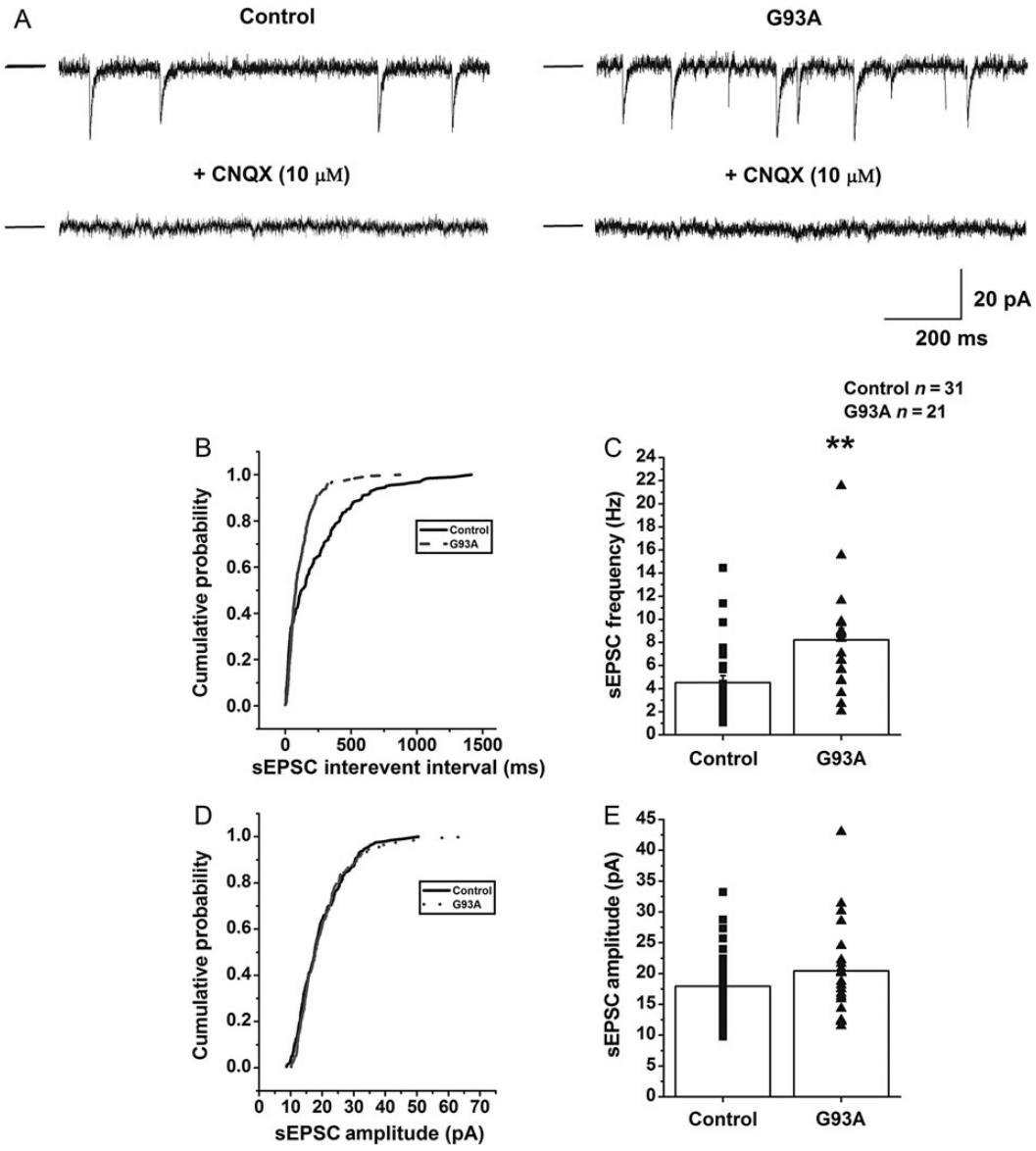

Figure 4. The G93A motor neurons show a significantly increased sEPSC frequency compared with the control. (*A*) Representative traces of sEPSCs in a control (left) and G93A (right) neuron. In the presence of CNQX (10 μM, Sigma), a non-NMDA receptor antagonist, the synaptic events were completely abolished in both neuronal populations. (*B*) Cumulative probability plots of IEIs of sEPSCs in the control and G93A neurons shown in A. In the G93A motor neuron, the IEI was significantly lower compared with the control neuron ($P < 0.01$; K–S test). (*C*) Bar plot of the sEPSC frequency means and standard errors in the control and G93A neurons. (*D*) Cumulative amplitude distributions of the control and G93A sEPSCs shown in *A* ($P > 0.05$; K–S test). (*E*) Bar plot of the means and standard errors of the sEPSC amplitudes in the control (17.95 ± 1.03 pA, $n = 31$) and G93A (20.42 ± 1.68 pA, $n = 21$; $P > 0.05$ unpaired Student's *t*-test) neurons. **$P < 0.01$ unpaired Student's *t*-test.

system areas of ALS mouse models (Pieri et al. 2003; Kuo et al. 2005; van Zundert et al. 2008; Pieri et al. 2009; Carunchio et al. 2010; Nieto-Gonzalez et al. 2010; Thielsen et al. 2013) and ascribed to a reduction of the recovery time from the transient sodium current inactivation (Zona et al. 2006) and/or an upregulation of persistent inward sodium current (I_{Nap}) (Kuo et al. 2005; Pieri et al. 2009; Carunchio et al. 2010). Interestingly, I_{Nap}, which controls the threshold of neuronal excitability (Boehmer et al. 2000; Do and Bean 2003; Levin et al. 2006), is blocked by low doses of riluzole (Kuo et al. 2005; Pieri et al. 2009; Schuster et al. 2012). This drug, which is one of the most commonly used drugs in the treatment of ALS (Gordon 2011; Miller et al. 2012; Vucic, Lin et al. 2013), has also been reported to exert its neuroprotective effect by inhibiting the glutamatergic transmission, either at presynaptic level or postsynaptically (Frizzo et al. 2004; Wang et al. 2004; Cheah et al. 2010). The multiple effects of Riluzole, which all point to neuronal excitability reduction (Bellingham 2011), may explain its beneficial influence observed in the clinic, unlike anti-NMDA agents that have been reported to have no similar therapeutic effects (Pamphlett et al. 2003; de Carvalho et al. 2010). The higher EPSC frequency in the motor cortex, here firstly reported, is in line with the higher expression of N-type voltage-dependent calcium channels that was previously reported in G93A cultured cortical neurons (Pieri et al. 2013). These channels, together with P/Q-type calcium channels, preferentially interact with the release machinery in several central synapses with the consequence of triggering neurotransmitter release (Mintz et al. 1995; Qian and Noebels 2001; Cepeda

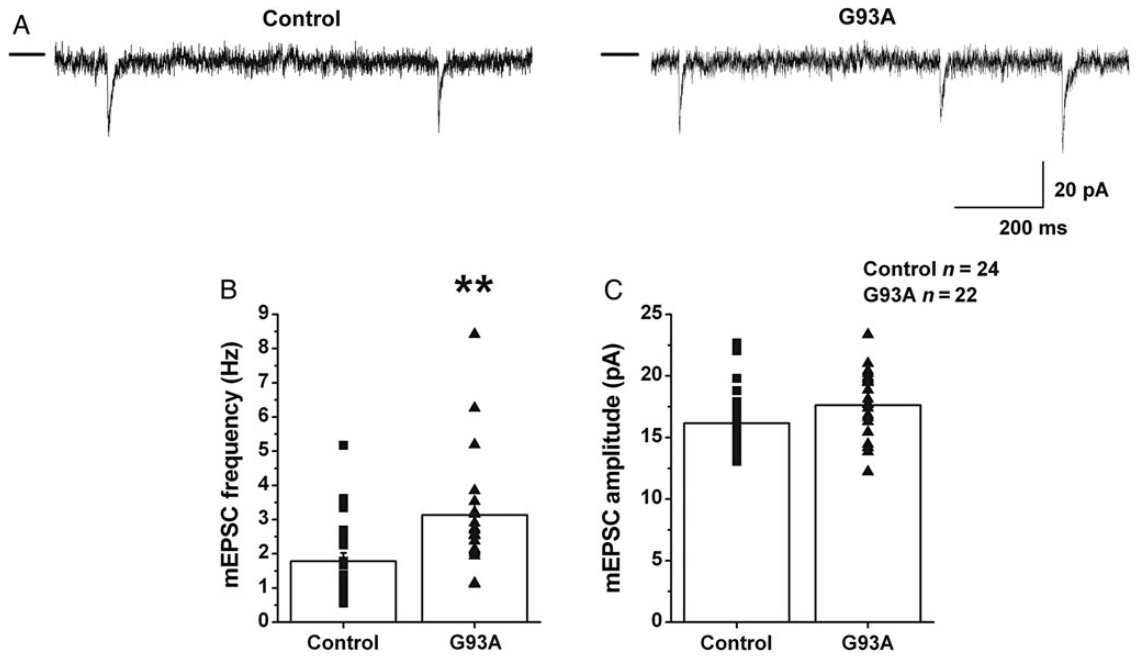

Figure 5. Recordings of mEPSCs in pyramidal neurons from the M1. (*A*) Representative traces of mEPSCs recorded in the control and G93A neurons. (*B*) Bar plot of the mEPSC frequency means and standard errors in the control and G93A neurons. (*C*) Bar plot of the means and standard errors of the mEPSC amplitudes in the control (16.15 ± 0.52 pA, $n = 24$) and G93A (17.61 ± 0.59 pA, $n = 22$; $P > 0.05$ unpaired Student's *t*-test) neurons. **$P < 0.01$ unpaired Student's *t*-test.

et al. 2004). Nevertheless, virtually nothing is known on how hyperexcitability impacts cortical glutamatergic transmission, including neurotransmitter release and vesicular glutamate packaging.

The higher frequency of EPSCs in G93A pyramidal motor neurons indicates an increase in glutamate release at the presynaptic level. The higher sEPSCs frequency observed in the ALS mouse model was not associated with significant differences of amplitude and kinetic properties, rise time, and decay time, which largely depend on the postsynaptic features of the recorded neurons. Furthermore, the facilitation of glutamate release in the G93A mice was independent of AP generation in the presynaptic neuronal terminals, since in G93A pyramidal motor neurons, the frequency of mEPSCs was still significantly higher than that in control. This indicates that the increased release of glutamate has only a synaptic origin.

The presynaptic glutamate release is finely regulated by VGluTs responsible for packaging glutamate into synaptic vesicles (Fremeau, Kam et al. 2004; Takamori 2006). VGluTs levels, which are critical for the balance between excitation and inhibition (Cline 2005; Erickson et al. 2006; Seal et al. 2008) and synaptic transmission (Wojcik et al. 2004; Fremeau, Voglmaier et al. 2004; Wilson et al. 2005), are altered in different pathological conditions. In fact, previous studies have reported that VGluTs expression levels are altered in pathologies such as depression (Moutsimilli et al. 2005; Tordera et al. 2005; Moutsimilli et al. 2008), schizophrenia (Eastwood and Harrison 2005; Uezato et al. 2009), Alzheimer's disease (Kirvell et al. 2006), and Parkinson's disease (Kashani et al. 2007). Moreover, the importance of the VGluT2 expression level has been reported in VGluT2 knockout mice, in which the total gene deletion induced perinatal lethality, whereas the heterozygous gene condition led to glutamatergic signaling deficit in the thalamus (Moechars et al. 2006). However, little is known about the role of VGluTs in the pathophysiology of ALS. Recently, it has been demonstrated that the genetic reduction of VGluT2 protein levels in G93A mice reduced motor neuron degeneration in the lumbar spinal cord of symptomatic mice but was ineffective in delaying the disease onset or increasing the life span, probably because too few motor neurons were rescued to affect disease progression (Wootz et al. 2010).

In this study, we showed for the first time that VGluT2 mRNA and protein levels were significantly enhanced in the M1 region of G93A mice, whereas VGluT1 levels were unaffected. Our immunohistological data then revealed that VGluT2 levels were increased only in M1 selective cortical layers, namely, Layers II/III and deep part of Layer V. Because VGluTs control the amount and probability of glutamate release (Fremeau, Voglmaier et al. 2004; Wilson et al. 2005; Takamori 2006), increased VGluT2 expression in Layers II–III and V of the G93A motor cortex is therefore consistent with the enhanced frequency of EPSCs of G93A corticomotor neurons lying in Layer V, although it is not possible to exclude an increased vesicular turnover. Furthermore, VGluT1 and VGluT2 are present at synapses located in different regions of the brain. VGluT1 pertains to cortical synapses, whereas VGluT2 is predominately present at thalamic synapses (Fremeau et al. 2001; Fujiyama et al. 2001). Thus, if VGluT1 and VGluT2 immunoreactivity can differentiate between synapses of cortical or thalamic origin (Fujiyama et al. 2001; Barroso-Chinea et al. 2007; Graziano et al. 2008; Hooks et al. 2013), an increase in VGluT2 should be expected to occur at thalamic synapses. However, our RT-PCR data question this prediction. In fact, considering that VGluTs mRNA is expressed in cell bodies and VGluTs proteins are expressed in axon terminals (Agis-Balboa et al. 2006), an enhancement of VGluT2 mRNA in the M1 region can suggest an enhanced intracortical transcriptional activity driving the increment of VGluT2 at the M1 synapses. However, since neurons expressing VGluT2 mRNA are a small minority of M1 neurons, we cannot exclude the fact that the observed increase of VGluT2 expression is the result of a combination of both intracortical and extracortical synaptic upregulation.

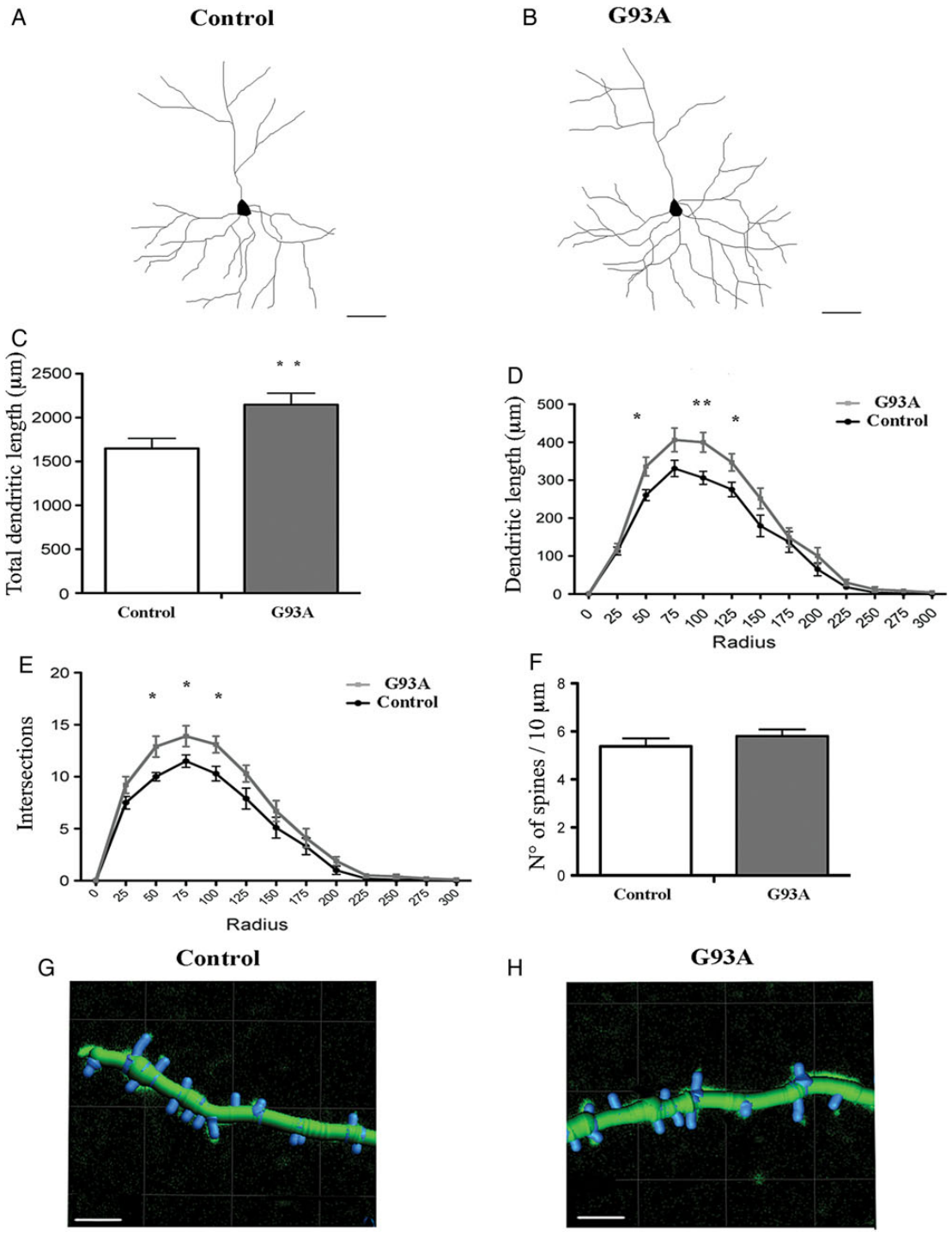

Figure 6. Representative images of 3D-reconstructed neurons of Layer V motor cortex in the control (*A*) and G93A (*B*) mice. (*C*) Histogram showing basal dendritic length of biocytin-filled neurons of deep portion of Layer V in M1 of control and G93A mice. In G93A mice, Layer V pyramidal neurons show a greater basal dendritic length compared with control (**$P < 0.01$; paired Student's *t*-test). (*D*,*E*) Graphs of Sholl analysis for Layer V pyramidal neuron basal dendritic length and number of intersections per 25-µm radial unit distance from the soma in the control and G93A mice. G93A mice present an increase in branching complexity at a radial distance of 50–125 µm relative to the soma (dendritic length: 50 µm $P < 0.05$, 100 µm $P < 0.01$, 125 µm $P < 0.05$; intersections: 50 µm $P < 0.05$, 75 µm $P < 0.05$, 100 µm $P < 0.05$). *$P < 0.05$; **$P < 0.01$; Student's *t*-test. (*F*) Histogram showing the mean spine density of pyramidal biocytin-filled neurons in control and G93A mice. Note that spine density of pyramidal biocytin-filled neurons of G93A and control mice is not significantly different ($P > 0.05$; Student's *t*-test). (*G*,*H*) Volume rendering of the maximum projection image created by Filament Tracer module of Imaris software package for spine density of Layer V pyramidal biocytin-filled neurons in control (*G*) and G93A (*H*) mice. Scale bars *A*,*B* = 50 µm; *G*,*H* = 5 µm.

Immunohistochemical and biochemical data need some consideration. To attempt quantification, it is always a risky business, and all techniques present limitations related to the tissue, antibodies, and fluorescence probes, and to the difficulties in delimiting areas of interest. To improve the significance of quantitative evaluations, we adopted 2 methods: immunohistochemistry and biochemistry. The first method provides high precision in anatomical definition but is somewhat questionable in

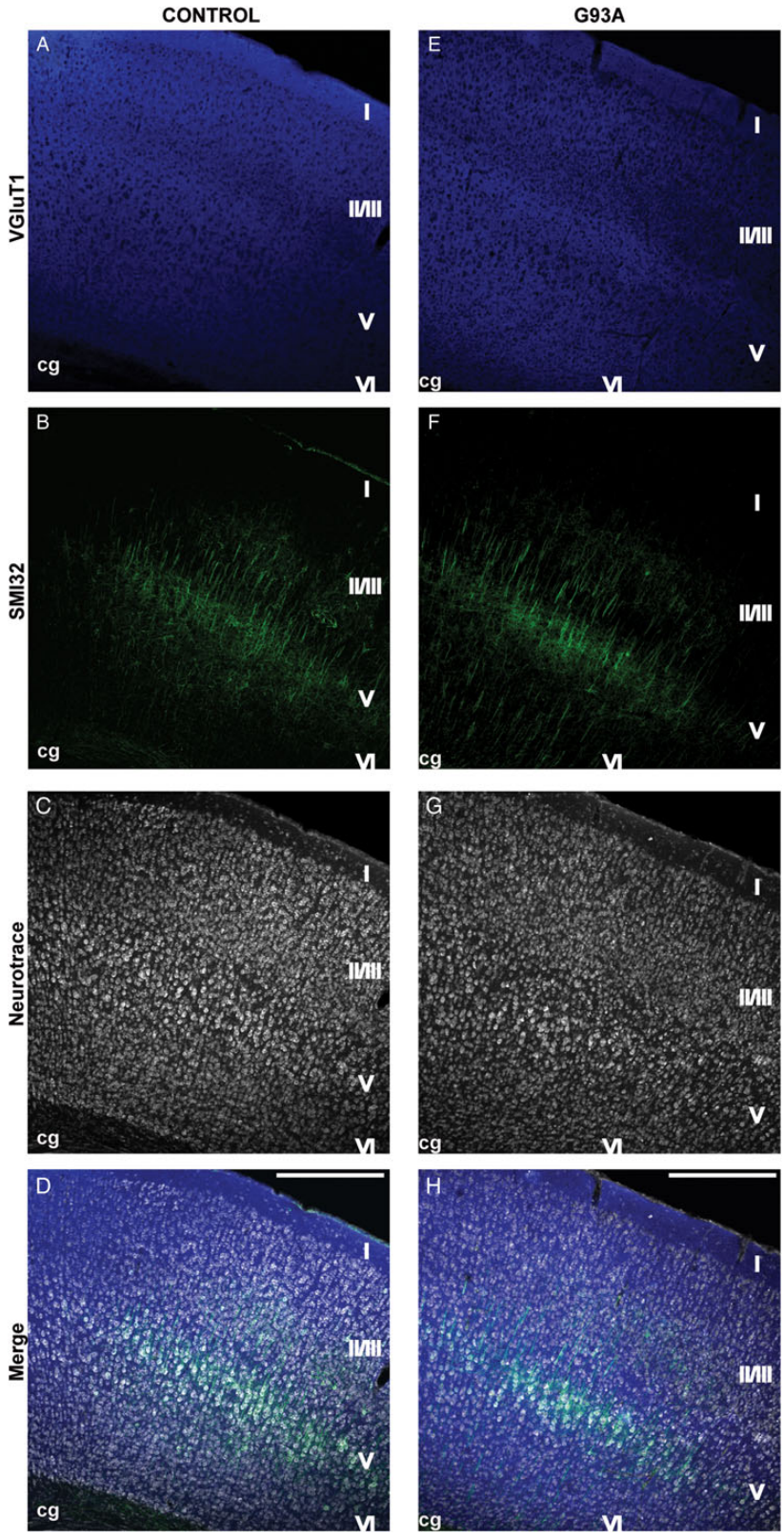

Figure 7. Distribution of VGluT1 in the different motor cortex (M1) layers of the control and G93A mice. Confocal images of triple immunofluorescence for VGluT1 (blue), SMI-32 (green), and Neurotrace (Nissl-fluorescent stain; gray) and merge in the control (*A–D*) and G93A (*E–H*) mice. Note the widespread VGluT1 immunoreactivity in all M1 layers of the control (*A*) and G93A mice (*E*). cg = cingulum. Scale bar (*A–H*) = 200 μm.

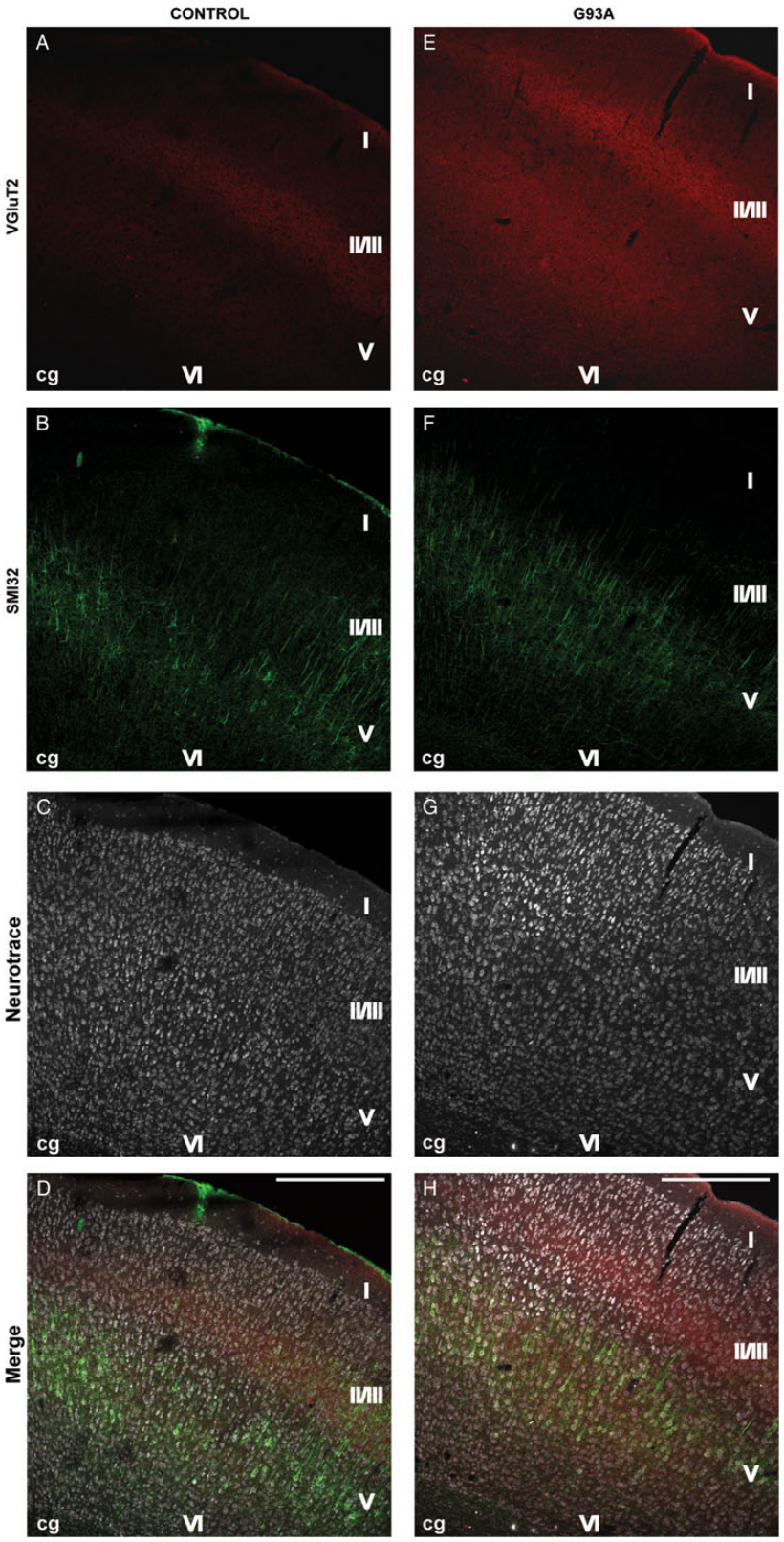

Figure 8. Distribution of VGluT2 in the different motor cortex (M1) layers of the control and G93A mice. Confocal images of triple immunofluorescence for VGluT2 (red), SMI-32 (green), and Neurotrace (Nissl-fluorescent stain; gray) and merge in the control (*A–D*) and G93A (*E–H*) mice. Note that VGluT2 immunoreactivity in the M1 presents significant differences between the 2 experimental groups. In the control, VGluT2 immunoreactivity is weak in almost all layers except in the deep portion of layers II/III (*A*). In the G93A mice, VGluT2 immunoreactivity is more intense compared with the control in almost all layers of M1 (*E*). In particular, in the G93A mice, the deep portion of Layers II/III and V of the M1, which appear densely SMI-32 labeled (*F–H*), showed a more intense VGluT2 immunoreactivity compared with the control. cg = cingulum. Scale bar (*A–H*) = 200 μm.

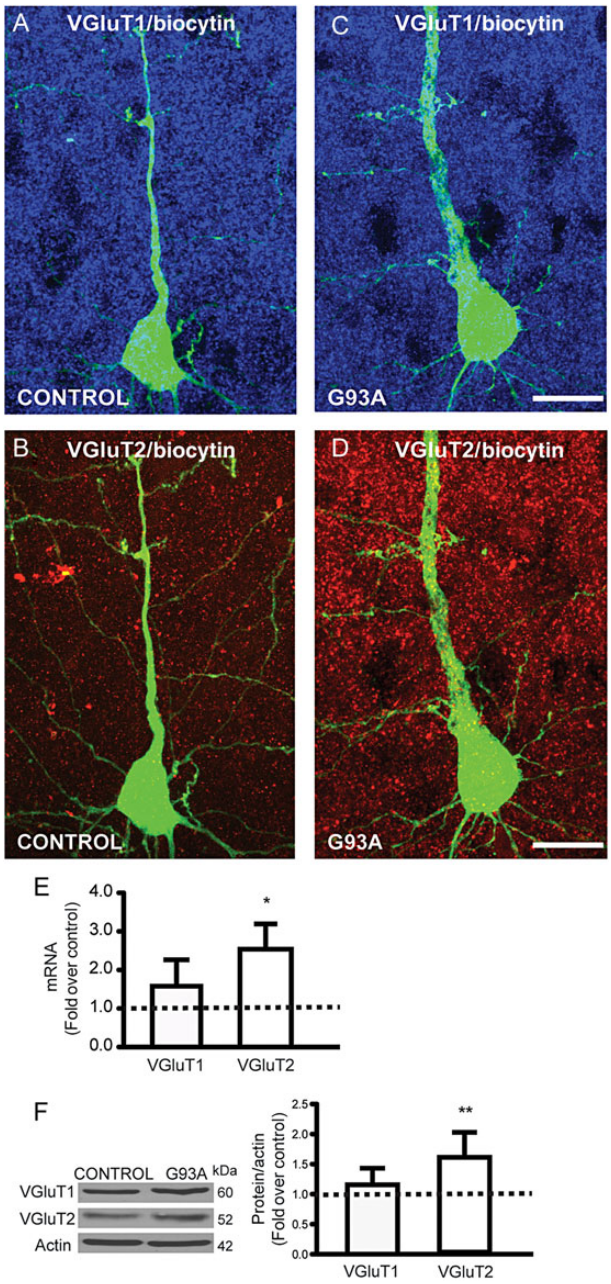

Figure 9. Immunohistochemical characterization and mRNA/protein expression of VGluT1 and VGluT2 in the motor cortex (M1) of the control and G93A biocytin-filled slices. (*A–D*) Confocal images of triple immunostaining showing biocytin-filled pyramidal cells of Layer V (green) surrounded by terminals immunoreactive for VGluT1 (blue) and VGluT2 (red) in the control (*A*,*B*) and G93A (*C*,*D*) mice. Note that VGluT1 is expressed by almost all synaptic terminals both in the control (*A*) and G93A (*C*) mice. Conversely, VGluT2 is expressed by few synaptic terminals in the control (*B*) and by a large number in the G93A mice (*D*). (*E*) Densitometric graphs of the VGluT1 and VGluT2 mRNA expression normalized to the internal control (ß-actin), in the control and G93A groups. (*F*) Representative immunoblots and densitometric graphs of VGluT1 and VGluT2 protein expression, normalized to the internal control (ß-actin), in the control and G93A groups. Note that the levels of VGluT1 mRNA and protein are not significantly different between the control and G93A groups. Conversely, the levels of VGluT2 mRNA and protein are significantly higher in the G93A mice compared with the control. $^{*}P < 0.05$; $^{**}P < 0.01$ paired Student's *t*-test. Scale bar (*A–D*) = 25 μm.

sensitivity. On the other hand, the second method may be questioned regarding precision in anatomical localization but is considered quite reliable regarding quantification. In our study, both methods presented convergent results, thus providing quite compelling evidence of the characteristic pattern of VGluT2 expression in M1 of G93A mice.

In line with data that showed that the complexity of dendritic arborization is regulated by neuronal activity and trophic factors during the course of development (Libersat and Duch 2004; Tripodi et al. 2008) and that the number of synaptic inputs is strictly related to the extension of dendritic arborization (Harris et al. 2003), hyperexcitable neurons exhibited morphological alterations in the direction of a structural gain of function. In particular, although our results indicate that the spine density was not modified in the mutated neurons compared with control, we observed that the basal dendrites of Layer V motor neurons, receiving excitatory inputs from local sources from the same and/or adjacent areas (Hooks et al. 2013; Petersen and Crochet 2013; Shepherd 2013), were longer and exhibited more ramifications, indicating an enhanced cortical connectivity in the early stage of the disease. Some previous reports have shown that dendrite arborization is increased in the lumbar motor neurons of G93A mice early (P4–P9) in development (Amendola and Durand 2008), whereas others have shown that it is decreased in cortical motor neurons of older (3 months) G93A mice (Spalloni et al. 2010). Our pattern of results is therefore consistent with a scenario in which the early detected enhancement of neuronal activity in motor neurons might initially trigger an increase of connectivity in G93A motor circuits. Then, the parallel activation of glutamate release, revealed by the enhancement of the VGluT2 level, detected in the very presymptomatic mouse age, would increase excitotoxicity in the motor neuron environment and then produce the opposite structural alterations, starting from a reduction of dendrite arborization in older mice (Spalloni et al. 2010) until neuronal loss (Seijffers et al. 2014).

It is therefore evident that the exacerbated dendritic arborization, the increased expression of VGluT2, and the hyperexcitability in the M1 Layer V neurons, all events observed at a very early stage of the disease, represent concomitant factors highly favorable to the enhancement of glutamate release, inducing its accumulation in the M1 region and, consequently, causing the excitotoxic neuronal death (Kim et al. 2012). In fact, as a consequence of all that has been reported, the greater glutamate release may lead to higher glutamate levels at the synaptic clefts, further exacerbated by the decreased levels of glial excitatory amino acid transporter-2 (EAAT2/GLT-1), previously observed both in the motor cortex and spinal cord from ALS patients (Rothstein 1995; Lin et al. 1998) and confirmed in ALS mouse models (Bruijn et al. 1997; Rothstein et al. 2005; Foran and Trotti 2009; Foran et al. 2011; Morel et al. 2013). In alternative, the decreased EAAT2/GLT-1 expression reported in ALS may cause higher levels of synaptic glutamate, with a consequent increase of EPSC frequency and upregulation of VGluT2 expression.

Our findings demonstrate for the first time the existence of early profound alterations in glutamatergic neurotransmission, associated with modified VGluT2 expression and neuronal morphology in the ALS motor cortex. These alterations indicate that the cortical area has a fundamental role in ALS disease onset and progression and should thus be taken into account for the treatment of this neurodegenerative disease.

Supplementary Material

Supplementary material can be found at: http://www.cercor.oxfordjournals.org/.

Funding

We thank the Thierry Latran Foundation for funding this work.

Notes

We thank Dr Alessia Antonini for input and suggestions, Prof. Diego Centonze for the critical reading of this manuscript. The professional editorial work of the Nature Publishing Group Language Editing is also acknowledged. *Conflict of Interest*: None declared.

References

Agis-Balboa RC, Pinna G, Zhubi A, Maloku E, Veldic M, Costa E, Guidotti A. 2006. Characterization of brain neurons that express enzymes mediating neurosteroid biosynthesis. Proc Natl Acad Sci USA. 103:14602–14607.

Alexianu ME, Kozovska M, Appel SH. 2001. Immune reactivity in a mouse model of familial ALS correlates with disease progression. Neurology. 57:1282–1289.

Amendola J, Durand J. 2008. Morphological differences between wild-type and transgenic superoxide dismutase 1 lumbar motoneurons in postnatal mice. J Comp Neurol. 511:329–341.

Andersen PM. 2006. Amyotrophic lateral sclerosis associated with mutations in the CuZn superoxide dismutase gene. Curr Neurol Neurosci Rep. 6:37–46.

Barroso-Chinea P, Castle M, Aymerich MS, Perez-Manso M, Erro E, Tunon T, Lanciego JL. 2007. Expression of the mRNAs encoding for the vesicular glutamate transporters 1 and 2 in the rat thalamus. J Comp Neurol. 501:703–715.

Beauchamp C, Fridovich I. 1971. Superoxide dismutase: improved assays and an assay applicable to acrylamide gels. Anal Biochem. 44:276–287.

Bellingham MC. 2011. A review of the neural mechanisms of action and clinical efficiency of riluzole in treating amyotrophic lateral sclerosis: what have we learned in the last decade? CNS Neurosci Ther. 17:4–31.

Boehmer G, Greffrath W, Martin E, Hermann S. 2000. Subthreshold oscillation of the membrane potential in magnocellular neurones of the rat supraoptic nucleus. J Physiol. 526(Pt 1):115–128.

Bogaert E, d'Ydewalle C, Van Den Bosch L. 2010. Amyotrophic lateral sclerosis and excitotoxicity: from pathological mechanism to therapeutic target. CNS Neurol Disord Drug Targets. 9:297–304.

Bruijn LI, Becher MW, Lee MK, Anderson KL, Jenkins NA, Copeland NG, Sisodia SS, Rothstein JD, Borchelt DR, Price DL, et al. 1997. ALS-linked SOD1 mutant G85R mediates damage to astrocytes and promotes rapidly progressive disease with SOD1-containing inclusions. Neuron. 18:327–338.

Carunchio I, Curcio L, Pieri M, Pica F, Caioli S, Viscomi MT, Molinari M, Canu N, Bernardi G, Zona C. 2010. Increased levels of p70S6 phosphorylation in the G93A mouse model of amyotrophic lateral sclerosis and in valine-exposed cortical neurons in culture. Exp Neurol. 226:218–230.

Cepeda C, Starling AJ, Wu N, Nguyen OK, Uzgil B, Soda T, Andre VM, Ariano MA, Levine MS. 2004. Increased GABAergic function in mouse models of Huntington's disease: reversal by BDNF. J Neurosci Res. 78:855–867.

Cheah BC, Vucic S, Krishnan AV, Kiernan MC. 2010. Riluzole, neuroprotection and amyotrophic lateral sclerosis. Curr Med Chem. 17:1942–1959.

Cline H. 2005. Synaptogenesis: a balancing act between excitation and inhibition. Curr Biol. 15:R203–R205.

de Carvalho M, Pinto S, Costa J, Evangelista T, Ohana B, Pinto A. 2010. A randomized, placebo-controlled trial of memantine for functional disability in amyotrophic lateral sclerosis. Amyotroph Lateral Scler. 11:456–460.

Deng HX, Hentati A, Tainer JA, Iqbal Z, Cayabyab A, Hung WY, Getzoff ED, Hu P, Herzfeldt B, Roos RP, et al. 1993. Amyotrophic lateral sclerosis and structural defects in Cu,Zn superoxide dismutase. Science. 261:1047–1051.

Do MT, Bean BP. 2003. Subthreshold sodium currents and pacemaking of subthalamic neurons: modulation by slow inactivation. Neuron. 39:109–120.

Eastwood SL, Harrison PJ. 2005. Decreased expression of vesicular glutamate transporter 1 and complexin II mRNAs in schizophrenia: further evidence for a synaptic pathology affecting glutamate neurons. Schizophr Res. 73:159–172.

Erickson JD, De Gois S, Varoqui H, Schafer MK, Weihe E. 2006. Activity-dependent regulation of vesicular glutamate and GABA transporters: a means to scale quantal size. Neurochem Int. 48:643–649.

Foran E, Bogush A, Goffredo M, Roncaglia P, Gustincich S, Pasinelli P, Trotti D. 2011. Motor neuron impairment mediated by a sumoylated fragment of the glial glutamate transporter EAAT2. Glia. 59:1719–1731.

Foran E, Trotti D. 2009. Glutamate transporters and the excitotoxic path to motor neuron degeneration in amyotrophic lateral sclerosis. Antioxid Redox Signal. 11:1587–1602.

Franklin KJ, Paxinos G. 1997. The Mouse Brain in Stereotaxic Coordinates. San Diego: Academic Press.

Fremeau RT, Kam K, Qureshi T, Johnson J, Copenhagen DR, Storm-Mathisen J, Chaudhry FA, Nicoll RA, Edwards RH. 2004. Vesicular glutamate transporters 1 and 2 target to functionally distinct synaptic release sites. Science. 304:1815–1819.

Fremeau RT, Troyer MD, Pahner I, Nygaard GO, Tran CH, Reimer RJ, Bellocchio EE, Fortin D, Storm-Mathisen J, Edwards RH. 2001. The expression of vesicular glutamate transporters defines two classes of excitatory synapse. Neuron. 31:247–260.

Fremeau RT, Voglmaier S, Seal RP, Edwards RH. 2004. VGLUTs define subsets of excitatory neurons and suggest novel roles for glutamate. Trends Neurosci. 27:98–103.

Frizzo ME, Dall'Onder LP, Dalcin KB, Souza DO. 2004. Riluzole enhances glutamate uptake in rat astrocyte cultures. Cell Mol Neurobiol. 24:123–128.

Fujiyama F, Furuta T, Kaneko T. 2001. Immunocytochemical localization of candidates for vesicular glutamate transporters in the rat cerebral cortex. J Comp Neurol. 435:379–387.

Gordon PH. 2011. Amyotrophic lateral sclerosis: pathophysiology, diagnosis and management. CNS Drugs. 25:1–15.

Graziano A, Liu XB, Murray KD, Jones EG. 2008. Vesicular glutamate transporters define two sets of glutamatergic afferents to the somatosensory thalamus and two thalamocortical projections in the mouse. J Comp Neurol. 507:1258–1276.

Grosskreutz J, Haastert K, Dewil M, Van Damme P, Callewaert G, Robberecht W, Dengler R, Van Den Bosch L. 2007. Role of mitochondria in kainate-induced fast Ca2+ transients in cultured spinal motor neurons. Cell Calcium. 42:59–69.

Guatteo E, Carunchio I, Pieri M, Albo F, Canu N, Mercuri NB, Zona C. 2007. Altered calcium homeostasis in motor neurons following AMPA receptor but not voltage-dependent calcium channels' activation in a genetic model of amyotrophic lateral sclerosis. Neurobiol Dis. 28:90–100.

Gurney ME. 1994. Transgenic-mouse model of amyotrophic lateral sclerosis. N Engl J Med. 331:1721–1722.

Harris KM, Fiala JC, Ostroff L. 2003. Structural changes at dendritic spine synapses during long-term potentiation. Philos Trans R Soc Lond B Biol Sci. 358:745–748.

Hooks BM, Mao T, Gutnisky DA, Yamawaki N, Svoboda K, Shepherd GM. 2013. Organization of cortical and thalamic input to pyramidal neurons in mouse motor cortex. J Neurosci. 33:748–760.

Kashani A, Betancur C, Giros B, Hirsch E, El Mestikawy S. 2007. Altered expression of vesicular glutamate transporters VGLUT1 and VGLUT2 in Parkinson disease. Neurobiol Aging. 28:568–578.

Kiernan MC, Vucic S, Cheah BC, Turner MR, Eisen A, Hardiman O, Burrell JR, Zoing MC. 2011. Amyotrophic lateral sclerosis. Lancet. 377:942–955.

Kim HJ, Kim TH, Choi SJ, Hong YJ, Yang JS, Sung KW, Rhie DJ, Hahn SJ, Yoon SH. 2012. Fluoxetine suppresses synaptically induced [Ca(2)(+)]i spikes and excitotoxicity in cultured rat hippocampal neurons. Brain Res. 1490:23–34.

Kirvell SL, Esiri M, Francis PT. 2006. Down-regulation of vesicular glutamate transporters precedes cell loss and pathology in Alzheimer's disease. J Neurochem. 98:939–950.

Kuo JJ, Siddique T, Fu R, Heckman CJ. 2005. Increased persistent Na(+) current and its effect on excitability in motoneurones cultured from mutant SOD1 mice. J Physiol. 563:843–854.

Levin SI, Khaliq ZM, Aman TK, Grieco TM, Kearney JA, Raman IM, Meisler MH. 2006. Impaired motor function in mice with cell-specific knockout of sodium channel Scn8a (NaV1.6) in cerebellar purkinje neurons and granule cells. J Neurophysiol. 96:785–793.

Libersat F, Duch C. 2004. Mechanisms of dendritic maturation. Mol Neurobiol. 29:303–320.

Lin CL, Bristol LA, Jin L, Dykes-Hoberg M, Crawford T, Clawson L, Rothstein JD. 1998. Aberrant RNA processing in a neurodegenerative disease: the cause for absent EAAT2, a glutamate transporter, in amyotrophic lateral sclerosis. Neuron. 20:589–602.

Maekawa S, Al-Sarraj S, Kibble M, Landau S, Parnavelas J, Cotter D, Everall I, Leigh PN. 2004. Cortical selective vulnerability in motor neuron disease: a morphometric study. Brain. 127:1237–1251.

Martorana F, Brambilla L, Valori CF, Bergamaschi C, Roncoroni C, Aronica E, Volterra A, Bezzi P, Rossi D. 2012. The BH4 domain of Bcl-X(L) rescues astrocyte degeneration in amyotrophic lateral sclerosis by modulating intracellular calcium signals. Hum Mol Genet. 21:826–840.

Miller RG, Mitchell JD, Moore DH. 2012. Riluzole for amyotrophic lateral sclerosis (ALS)/motor neuron disease (MND). Cochrane Database Syst Rev. 3:CD001447.

Mintz IM, Sabatini BL, Regehr WG. 1995. Calcium control of transmitter release at a cerebellar synapse. Neuron. 15:675–688.

Moechars D, Weston MC, Leo S, Callaerts-Vegh Z, Goris I, Daneels G, Buist A, Cik M, van der Spek P, Kass S, et al. ' 2006. Vesicular glutamate transporter VGLUT2 expression levels control quantal size and neuropathic pain. J Neurosci. 26:12055–12066.

Mogyoros I, Kiernan MC, Burke D. 1996. Strength-duration properties of human peripheral nerve. Brain. 119(Pt 2): 439–447.

Mogyoros I, Kiernan MC, Burke D, Bostock H. 1998. Strength-duration properties of sensory and motor axons in amyotrophic lateral sclerosis. Brain. 121(Pt 5):851–859.

Moreira LG, Pereira LC, Drummond PR, De Mesquita JF. 2013. Structural and functional analysis of human SOD1 in amyotrophic lateral sclerosis. PLoS One. 8:e81979.

Morel L, Regan M, Higashimori H, Ng SK, Esau C, Vidensky S, Rothstein J, Yang Y. 2013. Neuronal exosomal miRNA-dependent translational regulation of astroglial glutamate transporter GLT1. J Biol Chem. 288:7105–7116.

Moutsimilli L, Farley S, Dumas S, El Mestikawy S, Giros B, Tzavara ET. 2005. Selective cortical VGLUT1 increase as a marker for antidepressant activity. Neuropharmacology. 49:890–900.

Moutsimilli L, Farley S, El Khoury MA, Chamot C, Sibarita JB, Racine V, El Mestikawy S, Mathieu F, Dumas S, Giros B, et al. 2008. Antipsychotics increase vesicular glutamate transporter 2 (VGLUT2) expression in thalamolimbic pathways. Neuropharmacology. 54:497–508.

Nieto-Gonzalez JL, Moser J, Lauritzen M, Schmitt-John T, Jensen K. 2010. Reduced GABAergic inhibition explains cortical hyperexcitability in the wobbler mouse model of ALS. Cereb Cortex. 21:625–635.

Oswald MJ, Tantirigama ML, Sonntag I, Hughes SM, Empson RM. 2013. Diversity of layer 5 projection neurons in the mouse motor cortex. Front Cell Neurosci. 7:174.

Pamphlett R, Todd E, Vink R, McQuilty R, Cheema SS. 2003. Magnesium supplementation does not delay disease onset or increase survival in a mouse model of familial ALS. J Neurol Sci. 216:95–98.

Panov A, Kubalik N, Zinchenko N, Hemendinger R, Dikalov S, Bonkovsky HL. 2011. Respiration and ROS production in brain and spinal cord mitochondria of transgenic rats with mutant G93a Cu/Zn-superoxide dismutase gene. Neurobiol Dis. 44:53–62.

Petersen CC, Crochet S. 2013. Synaptic computation and sensory processing in neocortical layer 2/3. Neuron. 78:28–48.

Philips T, Robberecht W. 2011. Neuroinflammation in amyotrophic lateral sclerosis: role of glial activation in motor neuron disease. Lancet Neurol. 10:253–263.

Pieri M, Albo F, Gaetti C, Spalloni A, Bengtson CP, Longone P, Cavalcanti S, Zona C. 2003. Altered excitability of motor neurons in a transgenic mouse model of familial amyotrophic lateral sclerosis. Neurosci Lett. 351:153–156.

Pieri M, Caioli S, Canu N, Mercuri NB, Guatteo E, Zona C. 2013. Over-expression of N-type calcium channels in cortical neurons from a mouse model of amyotrophic lateral sclerosis. Exp Neurol. 247:349–358.

Pieri M, Carunchio I, Curcio L, Mercuri NB, Zona C. 2009. Increased persistent sodium current determines cortical hyperexcitability in a genetic model of amyotrophic lateral sclerosis. Exp Neurol. 215:368–379.

Qian J, Noebels JL. 2001. Presynaptic Ca2+ channels and neurotransmitter release at the terminal of a mouse cortical neuron. J Neurosci. 21:3721–3728.

Rosen DR, Siddique T, Patterson D, Figlewicz DA, Sapp P, Hentati A, Donaldson D, Goto J, O'Regan JP, Deng HX, et al. 1993. Mutations in Cu/Zn superoxide dismutase gene are associated with familial amyotrophic lateral sclerosis. Nature. 362:59–62.

Rothstein JD. 1995. Excitotoxicity and neurodegeneration in amyotrophic lateral sclerosis. Clin Neurosci. 3:348–359.

Rothstein JD, Patel S, Regan MR, Haenggeli C, Huang YH, Bergles DE, Jin L, Dykes Hoberg M, Vidensky S, Chung DS, et al. 2005. Beta-lactam antibiotics offer neuroprotection by increasing glutamate transporter expression. Nature. 433:73–77.

Schuster JE, Fu R, Siddique T, Heckman CJ. 2012. Effect of prolonged riluzole exposure on cultured motoneurons in a mouse model of ALS. J Neurophysiol. 107:484–492.

Seal RP, Akil O, Yi E, Weber CM, Grant L, Yoo J, Clause A, Kandler K, Noebels JL, Glowatzki E, et al. 2008. Sensorineural deafness

and seizures in mice lacking vesicular glutamate transporter 3. Neuron. 57:263–275.
Seijffers R, Zhang J, Matthews JC, Chen A, Tamrazian E, Babaniyi O, Selig M, Hynynen M, Woolf CJ, Brown RH Jr. 2014. ATF3 expression improves motor function in the ALS mouse model by promoting motor neuron survival and retaining muscle innervation. Proc Natl Acad Sci USA. 111:1622–1627.
Shepherd GM. 2013. Corticostriatal connectivity and its role in disease. Nat Rev Neurosci. 14:278–291.
Shobha K, Vijayalakshmi K, Alladi PA, Nalini A, Sathyaprabha TN, Raju TR. 2007. Altered in-vitro and in-vivo expression of glial glutamate transporter-1 following exposure to cerebrospinal fluid of amyotrophic lateral sclerosis patients. J Neurol Sci. 254:9–16.
Spalloni A, Nutini M, Longone P. 2011. Role of the N-methyl-d-aspartate receptors complex in amyotrophic lateral sclerosis. Biochim Biophys Acta. 1832:312–322.
Spalloni A, Origlia N, Sgobio C, Trabalza A, Nutini M, Berretta N, Bernardi G, Domenici L, Ammassari-Teule M, Longone P. 2010. Postsynaptic alteration of NR2A subunit and defective autophosphorylation of alphaCaMKII at threonine-286 contribute to abnormal plasticity and morphology of upper motor neurons in presymptomatic SOD1G93A mice, a murine model for amyotrophic lateral sclerosis. Cereb Cortex. 21:796–805.
Stuart GJ, Dodt HU, Sakmann B. 1993. Patch-clamp recordings from the soma and dendrites of neurons in brain slices using infrared video microscopy. Pflugers Arch. 423:511–518.
Stys PK. 2005. General mechanisms of axonal damage and its prevention. J Neurol Sci. 233:3–13.
Suter BA, Migliore M, Shepherd GM. 2013. Intrinsic electrophysiology of mouse corticospinal neurons: a class-specific triad of spike-related properties. Cereb Cortex. 23:1965–1977.
Takamori S. 2006. VGLUTs: “exciting” times for glutamatergic research? Neurosci Res. 55:343–351.
Thielsen KD, Moser JM, Schmitt-John T, Jensen MS, Jensen K, Holm MM. 2013. The Wobbler Mouse Model of Amyotrophic Lateral Sclerosis (ALS) displays hippocampal hyperexcitability, and reduced number of interneurons, but no presynaptic vesicle release impairments. PLoS One. 8:e82767.
Tordera RM, Pei Q, Sharp T. 2005. Evidence for increased expression of the vesicular glutamate transporter, VGLUT1, by a course of antidepressant treatment. J Neurochem. 94: 875–883.
Tripodi M, Evers JF, Mauss A, Bate M, Landgraf M. 2008. Structural homeostasis: compensatory adjustments of dendritic arbor geometry in response to variations of synaptic input. PLoS Biol. 6:e260.
Uezato A, Meador-Woodruff JH, McCullumsmith RE. 2009. Vesicular glutamate transporter mRNA expression in the medial temporal lobe in major depressive disorder, bipolar disorder, and schizophrenia. Bipolar Disord. 11:711–725.
Van Den Bosch L, Van Damme P, Bogaert E, Robberecht W. 2006. The role of excitotoxicity in the pathogenesis of amyotrophic lateral sclerosis. Biochim Biophys Acta. 1762:1068–1082.
van Zundert B, Peuscher MH, Hynynen M, Chen A, Neve RL, Brown RH Jr, Constantine-Paton M, Bellingham MC. 2008. Neonatal neuronal circuitry shows hyperexcitable disturbance in a mouse model of the adult-onset neurodegenerative disease amyotrophic lateral sclerosis. J Neurosci. 28:10864–10874.
Vance C, Rogelj B, Hortobagyi T, De Vos KJ, Nishimura AL, Sreedharan J, Hu X, Smith B, Ruddy D, Wright P, et al. 2009. Mutations in FUS, an RNA processing protein, cause familial amyotrophic lateral sclerosis type 6. Science. 323:1208–1211.
Vucic S, Cheah BC, Yiannikas C, Kiernan MC. 2011. Cortical excitability distinguishes ALS from mimic disorders. Clin Neurophysiol. 122:1860–1866.
Vucic S, Lin CS, Cheah BC, Murray J, Menon P, Krishnan AV, Kiernan MC. 2013. Riluzole exerts central and peripheral modulating effects in amyotrophic lateral sclerosis. Brain. 136:1361–1370.
Vucic S, Nicholson GA, Kiernan MC. 2008. Cortical hyperexcitability may precede the onset of familial amyotrophic lateral sclerosis. Brain. 131:1540–1550.
Vucic S, Ziemann U, Eisen A, Hallett M, Kiernan MC. 2013. Transcranial magnetic stimulation and amyotrophic lateral sclerosis: pathophysiological insights. J Neurol Neurosurg Psychiatry. 84:1161–1170.
Wang SJ, Wang KY, Wang WC. 2004. Mechanisms underlying the riluzole inhibition of glutamate release from rat cerebral cortex nerve terminals (synaptosomes). Neuroscience. 125: 191–201.
Wijesekera LC, Leigh PN. 2009. Amyotrophic lateral sclerosis. Orphanet J Rare Dis. 4:3.
Wilson NR, Kang J, Hueske EV, Leung T, Varoqui H, Murnick JG, Erickson JD, Liu G. 2005. Presynaptic regulation of quantal size by the vesicular glutamate transporter VGLUT1. J Neurosci. 25:6221–6234.
Wojcik SM, Rhee JS, Herzog E, Sigler A, Jahn R, Takamori S, Brose N, Rosenmund C. 2004. An essential role for vesicular glutamate transporter 1 (VGLUT1) in postnatal development and control of quantal size. Proc Natl Acad Sci USA. 101:7158–7163.
Wootz H, Enjin A, Wallen-Mackenzie A, Lindholm D, Kullander K. 2010. Reduced VGLUT2 expression increases motor neuron viability in Sod1(G93A) mice. Neurobiol Dis. 37:58–66.
Zilles K. 1985. The Cortex of the Rat. A Stereotaxic Atlas. Berlin: Springer.
Zona C, Pieri M, Carunchio I. 2006. Voltage-dependent sodium channels in spinal cord motor neurons display rapid recovery from fast inactivation in a mouse model of amyotrophic lateral sclerosis. J Neurophysiol. 96:3314–3322.